AD-A234 080

BRL

NUMERICAL SIMULATION OF REACTING FLOW
IN A THERMALLY CHOKED RAM ACCELERATOR—
MODEL DEVELOPMENT AND VALIDATION

MICHAEL J. NUSCA

DTIC
SELECTE
APR 26 1991
S B D

APRIL 1991

U.S. ARMY LABORATORY COMMAND

BALLISTIC RESEARCH LABORATORY
ABERDEEN PROVING GROUND, MARYLAND

NOTICES

REPORT DOCUMENTATION PAGE

Form Approved
OMB No 0704-0188

1. AGENCY USE ONLY *(Leave blank)*	2. REPORT DATE	3. REPORT TYPE AND DATES COVERED
	April 1991	Final. Mar-Sep 90.

4. TITLE AND SUBTITLE

Numerical Simulation of Reacting Flow in a Thermally Choked Ram Accelerator - Model Development and Validation

5. FUNDING NUMBERS

1L162618AH80

6. AUTHOR(S)

Michael J. Nusca

7. PERFORMING ORGANIZATION NAME(S) AND ADDRESS(ES)

8. PERFORMING ORGANIZATION REPORT NUMBER

9. SPONSORING / MONITORING AGENCY NAME(S) AND ADDRESS(ES)

Ballistic Research Laboratory
ATTN: SLCBR-DD-T
Aberdeen Proving Ground, MD 21005-5066

10. SPONSORING / MONITORING AGENCY REPORT NUMBER

BRL-TR-3222

11. SUPPLEMENTARY NOTES

12a. DISTRIBUTION / AVAILABILITY STATEMENT

Approved for public release; distribution is unlimited.

12b. DISTRIBUTION CODE

13. ABSTRACT *(Maximum 200 words)*

Computational fluid dynamics solutions of the Navier-Stokes equations have been applied to both non-reacting and reacting in-bore flowfields for a ram accelerator projectile launch system. In this system a projectile is injected at supersonic velocity into a stationary tube filled with a pressurized mixture of hydrocarbon, oxidizer and inert gases. After ignition, the shock system generated by the projectile can result in sustained combustion around and aft of the projectile. This energy release process which travels with the projectile also generates high pressures and imparts thrust to the projectile. Numerical simulations reveal in-bore flowfield details and provide a good comparison with measured launch tube wall pressures for both non-reacting and reacting flows and a 38mm system. Computations are also used to investigate a proposed 120mm ram accelerator system.

14. SUBJECT TERMS		15. NUMBER OF PAGES
Fluid Dynamics Ramjet Engines Hypervelocity Guns Subsonic Combustion Navier-Stokes Equations		56
		16. PRICE CODE

17. SECURITY CLASSIFICATION OF REPORT	18. SECURITY CLASSIFICATION OF THIS PAGE	19. SECURITY CLASSIFICATION OF ABSTRACT	20. LIMITATION OF ABSTRACT
UNCLASSIFIED	UNCLASSIFIED	UNCLASSIFIED	SAR

NSN 7540-01-280-5500

Standard Form 298 (Rev 2-89)
Prescribed by ANSI Std 239-18
298-102

INTENTIONALLY LEFT BLANK.

Acknowledgement

The author wishes to acknowledge Mr. D. Kruczynski, Dr. T. Minor, Mr. A. Horst, Internal Ballistics Division and Dr. W. D'Amico, Launch and Flight Division, U.S. Army BRL, for their substantial support of this work.

INTENTIONALLY LEFT BLANK.

Table of Contents

INTENTIONALLY LEFT BLANK.

List of Figures

List of Tables

ix

INTENTIONALLY LEFT BLANK.

I. INTRODUCTION

Experimental testing and gasdynamic modeling of the ram acceleration technique for in-bore projectile propulsion[1-5] has been initiated at the U.S. Army Ballistic Research Laboratory (BRL) under the Hybrid Inbore RAM (HIRAM) propulsion program.[6] Numerical solutions of the Navier-Stokes equations have been obtained via computational fluid dynamics (CFD) for non-reacting and reacting flows.[7] Numerical simulations can be used as a system design aid and as a means by which geometric and fluid dynamic scaling phenomena are investigated. Reacting flows considered in this report include the thermally choked, subsonic combustion ram acceleration mode.

For non-reacting flow simulations the Rockwell Science Center USA-PG (Unified Solution Algorithm Perfect Gas) code[8,9] is used. In this code the Navier-Stokes equations are cast in conservation form and converted into a set of algebraic equations using upwind and central finite differences, finite-volume formulations and a second-order TVD (total variation diminishing) scheme. The code is capable of simulating mixed subsonic/supersonic flowfields. The USA-PG code has been used by the BRL to investigate solid-fuel ramjet projectiles.[10] For ram accelerator simulations the USA-PG code was run using inviscid, laminar, and turbulent/separated flow modes thus, viscous flow effects such as turbulent wall boundary layers and wake flow mixing are investigated. Flowfield shock wave generation and reflection patterns are computed. Fluid dynamic scaling phenomena associated with scaled-up projectile geometries (i.e. 38mm to 120mm) are investigated as well. Computed ram accelerator tube wall pressures are compared to data measured at the University of Washington using a 38mm system and inert gas mixtures.

For the reacting flow simulations the BRL-LFD RAMCOMB (RAMjet COMBustion) code[11] (solid fuel diffusion-flame technique) was modified for premixed gaseous fuel

[1] Bruckner, A.P., Bogdanoff, D.W., Knowlen, C., and Hertzberg, A., "Investigation of Gasdynamic Phenomena Associated with the Ram Accelerator Concept," AIAA-87-1327, Proceedings of the AIAA 19th Fluid Dynamics, Plasma Dynamics and Lasers Conference, June 8-10, 1987, Honolulu, Hawaii.

[2] Hertzberg, A., Bruckner, A.P., and Bogdanoff, D.W., "Ram Accelerator: A New Chemical Method for Accelerating Projectiles to Ultrahigh Velocities," AIAA Journal, Vol. 26, No. 2, Feb. 1988, pp. 195-203.

[3] Bruckner, A.P., Knowlen, C., Scott, K.A., and Hertzberg, A., "High Velocity Modes of the Thermally Choked Ram Accelerator," AIAA-88-2925, Proceedings for the AIAA 24th Joint Propulsion Conference July 11-13, 1988, Boston, MA.

[4] Burnham, E.A., Kull, A.E., Knowlen, C., Bruckner, A.P., and Hertzberg, A., "Operation of the Ram Accelerator in the Transdetonative Velocity Regime," AIAA-90-1985, Proceedings for the AIAA 26th Joint Propulsion Conference, July 16-18, 1990, Orlando, FL.

[5] Bruckner, Hertzberg, A., and Knowlen, C., "Review of Ram Accelerator Propulsion Modes," Proceedings of the 27th JANNAF Combustion Subcommittee Meeting, November 5-9, 1990, Warren AFB, Cheyenne, WY.

[6] Kruczynski, D.L., "Large Caliber Applications of Ram Accelerator Technology," Proceedings of the 27th JANNAF Combustion Subcommittee Meeting, November 5-9, 1990, Warren AFB, Cheyenne, WY.

[7] Nusca, M.J., "Numerical Simulation of Reacting Flow in a Thermally Choked Ram Accelerator," Proceedings of the 27th JANNAF Combustion Subcommittee Meeting, November 5-9, 1990, Warren AFB, Cheyenne, WY.

[8] Chakravarthy, S.R., Szema, K.Y., Goldberg, U.C., Gorski, J.J., and Osher, S., "Application of a New Class of High Accuracy TVD Schemes to the Navier-Stokes Equations," AIAA-85-0165, Proceedings of the AIAA 23rd Aerospace Sciences Meeting, Jan. 14-17, 1985, Reno, NV.

[9] Chakravarthy, S.R., Szema, K.Y., and Haney, J.W., "Unified Nose-to-Tail Computational Method for Hypersonic Vehicle Applications," AIAA-89-2564, Proceedings of the AIAA 6th Applied Aerodynamics Conference, June 6-8, 1989, Williamsburg, VA.

[10] Nusca, M.J., Chakravarthy, S.R., Goldberg, U.C., "Computational Fluid Dynamics Capability for the Solid-Fuel Ramjet Projectile," AIAA Journal of Propulsion and Power, Vol. 6, No. 3, May-June 1990, pp. 256-262 (see also AIAA-87-2411 and BRL-TR-2958, Dec. 1988).

[11] Nusca, M.J., "Steady Flow Combustion Model for Solid-Fuel Ramjet Projectiles," AIAA Journal of Propulsion and Power, Vol. 6, No. 3, May-June 1990, pp. 348-352 (see also AIAA-89-2797 and BRL-TR-2987, April 1989).

combustion. The steady 2D/axisymmetric Navier-Stokes equations are written in stream function-vorticity form and solved using a Gauss-Seidel relaxation scheme. These equations include conservation of chemical species and reacting flow source terms in the energy equation. A one-step, global, temperature and mass controlled, finite-rate reaction between fuel (CH_4) and oxidizer (O_2) is considered. The products of this reaction (e.g. CO_2 and H_2O) are lumped into one specie with mass-averaged thermodynamic properties. Diluent species (reactants and products) are also considered. Reaction rates are defined using the Law of Mass Action and Arrhenius expressions. Constants in the rate expressions as well as the molar specific enthalpy, heat of formation, specific heat, and molecular weight of the species are extracted from previous studies of hydrocarbon reactions. Upstream subsonic flow conditions for the reacton zone are obtained using the USA-PG code.

II. BACKGROUND

The ram accelerator technique was first investigated via experimental test firings at the University of Washington (UW).[1-5] The UW ram accelerator facility (Figure 1) uses a light gas gun (e.g. helium driver gas) to accelerate projectiles up to 1300 m/s. The muzzle is connected to a perforated tube and evacuation tank which serve as a dump for the driver gas prior to entrance into the 16m ram accelerator tube. This tube, which can be divided into sections separated by diaphragms, is filled with a pressurized fuel/oxidizer mixture and is instrumented at 40 axial locations. Instrumentation consists of pressure transducers, fiber-optic light guides, and magnetic transducers. Thin magnetic sheets are mounted in the nose-body joint and in the base of the projectile (see Figure 1). When the projectile passes electromagnetic transducers on the accelerator tube, these magnets induce signals that are used to determine the distance-time history (i.e. velocity) of the projectile.

The projectile consists of an axisymmetric cone-boattail body with stabilizing fins to center it along the launch tube axis (see Figure 2, fins excluded). The projectile is shaped like the centerbody of a ramjet engine and is injected into a stationary tube filled with a pressurized gas mixture of hydrocarbon fuel (e.g. CH_4), oxidizer and diluents such as CO_2, N_2, He, and Ar. There is no propellant on board the projectile. The tube resembles the outer cowling of a conventional ramjet engine. When the injection velocity is greater than the sound speed of the gas an oblique shock system develops on the projectile which can sustain combustion on the surface and aft of the projectile. In this way the energy release process travels behind the projectile. Thrust is generated by the action of high pressure reacting gases on the rear part of the projectile. Various combustion ignition mechanisms have been used. The initial gas pressure, fuel/oxidizer composition, and sound speed can be selected to achieve the desired acceleration and projectile velocity at tube exit. Diluents are used to tailor the acoustic speed of the mixture so that the initial Mach number of the projectile exceeds the minimum required ($\simeq 2.8$) to start the diffuser (i.e. the minimum projectile/tube clearance at maximum projectile body diameter) and tailors the heat release of combustion to a level that stabilizes the shock system on the projectile body. Excessive diluent results in low projectile acceleration levels, whereas insufficient diluent concentration can cause pre-ignition forward of the projectile.

2

The balance of forces on the projectile is composed of the drag force on the forebody and a thrust force produced by the high pressure combustion products on the projectile afterbody. Normally a net thrust is obtained since the pressure of the combustion products is higher than the compressed gases downstream of the nose shock. Gas mixtures with higher heat of reaction yield greater net thrust. Combustion must begin on the afterbody of the projectile in order to maximize the thrust. If combustion starts on the conical nose, the high pressure due to the reaction products will contribute to drag forces and thus, will reduce the net thrust. Similarly, if combustion starts aft of the cone-boattail junction on the projectile, then only a fraction of the afterbody area will be exposed to the high pressure gases and the thrust will be below its full potential value.

Several modes of ram accelerator operation have been investigated including thermally choked, transdetonative, oblique detonation wave, and superdetonative. These modes are distinguished by operating velocity and the manner in which the combustion process is initiated and sustained. The thermally choked, subsonic combustion mode will theoretically allow projectile acceleration up to the Chapman-Jouguet (C-J)* detonation speed of the gaseous propellant mixture. Operating modes that involve supersonic combustion have demonstrated acceleration beyond the C-J speed.[5] Numerical simulation of ram accelerator flowfields has been documented for supersonic flow such as the oblique detonation wave and superdetonative modes.[12-15] This report describes CFD modeling of 38mm and 120mm ram accelerator systems for non-reacting and reacting gas mixtures in the subsonic flow thermally choked mode.

Demonstrations of thermally choked ram acceleration at the University of Washington have achieved velocities up to 2.5 km/s in a 38mm diameter tube with a projectile mass of about 70g. A projectile is injected into the accelerator tube at 700-1200 m/s. The forebody angle of the projectile is such that the oblique shock system does not initiate combustion. A normal shock is located downstream of the maximum cross-sectional area of the projectile (Fig. 3); theoretically this shock is also not strong enough to ignite the gas mixture[3] provided that the projectile velocity does not exceed about Mach 4. Combustion is initiated immediately behind the projectile upon entrance to the ram accelerator tube (a published discussion of ignition is forthcoming from UW). The base of the projectile can act as a flameholder. The combustion zone spreads to the full diameter of the tube and reaches a thermal choking condition some distance downstream of the projectile. Thermal choking and the heat release due to combustion stabilizes the normal shock. In principle the concept is scalable for projectile mass in kilograms. Verification of the scaling principles is underway at the BRL using both experiments[6] and numerical simulations.[7]

* A normal shock in a constant area duct followed by heat addition and thermal choking in steady flow constitutes a C-J detonation wave.

[12] Bogdanoff, D.W., and Brackett, D.C., "A Computational Fluid Dynamics Code for the Investigation of Ramjet-in-Tube Concepts," AIAA-87-1978, Proceedings of the AIAA 23rd Joint Propulsion Conference, June 29-July 2, 1987, San Diego, CA.

[13] Yungster, S., Eberhardt, S., and Bruckner, A.P., "Numerical Simulation of Shock-Induced Combustion Generated by High-Speed Projectiles in Detonable Gas Mixtures," AIAA-89-0673, Proceedings of the AIAA 27th Aerospace Sciences Meeting, Jan. 9-12, 1989, Reno, NV.

[14] Yungster, S., and Bruckner, A.P., "A Numerical Study of the Ram Accelerator Concept in the Superdetonative Velocity Range," AIAA-89-2677, Proceedings of the AIAA 25th Joint Propulsion Conference, July 10-12, 1989, Monterey, CA.

[15] Chuck, C., and Eberhardt, S., "Numerical Simulation of Hypersonic Oblique Shock-Wave/Laminar Boundary-Layer Interaction with Shock Induced Combustion," AIAA-90-0149, Proceedings of the AIAA 28th Aerospace Sciences Meeting, Jan. 8-11, 1990, Reno, NV.

III. NON-REACTING FLOW

The CFD approach described in this section can be used to predict the compressible flowfield around aerodynamic bodies by solving two-dimensional (2D) and three-dimensional (3D) Reynolds-averaged Navier-Stokes (RANS) equations. The USA-PG2 and USA-PG3 codes were developed by Chakravarthy.[8,9] The Navier-Stokes equations are written using the perfect gas assumption however, versions of the code for a real gas have been documented as well.[16,17] Both laminar and turbulent flows can be investigated thus, a turbulence model[18] is required for closure. In addition, backflow regions can be present thus, a backflow turbulence model[19] is included. The equations are transformed into conservation law form and discretized using finite-volume approximations. The USA-PG code uses a class of numerical algorithms termed total variational diminishing (TVD) which do not require the inclusion of explicit smoothing or global dissipation functions to achieve numerical stability. The resulting set of equations is solved using an implicit, factored, time-stepping algorithm. The solution takes place on a computational grid that is generated around the configuration in zones; zonal boundaries are transparent to the flowfield.

The ram accelerator projectile geometry shown in Figure 2 represents a simplification of the actually configuration used for test firings. The actual projectile includes a set of four bore-riding fins that extend from the point of maximum projectile diameter to the projectile base and span the area between the projectile and the launch tube (see Figure 1). Exclusion of these fins permits a 2D/axisymmetric calculation and results in a significant computer time savings over the full 3D numerical simulation. Such 3D simulations are possible with the present code (e.g. see Reference 9); application to the ram accelerator will be addressed in future reports.

1. Equations of Motion.

The RANS equations for 2D/axisymmetric flow are written in the following conservation form. The dependent variables u, v and e are mass-averaged.

$$\frac{\partial W}{\partial t} + \frac{\partial F}{\partial x} + \frac{\partial G}{\partial y} + \left(\frac{G}{y} - \frac{H}{y}\right)\alpha = 0 \tag{1}$$

---

[16] Ota, D.K., Chakravarthy S.R., and Darling, J.C., "An Equilibrium Air Navier-Stokes Code for Hypersonic Flows," AIAA-88-0419, Proceedings of the 26th AIAA Aerospace Sciences Meeting, Reno, NV, January 11-14, 1988.

[17] Palaniswamy, S., and Chakravarthy, S.R., "Finite Rate Chemistry for USA Series Codes: Formulation and Applications," AIAA-89-0200, Proceedings of the 27th AIAA Aerospace Sciences Meeting, Reno. NV, January 9-12, 1989.

[18] Baldwin, B.S. and Lomax, H., "Thin Layer Approximation and Algebraic Model for Separated Turbulent Flows," AIAA-78-257, Proceedings of the 16th AIAA Aerospace Sciences Meeting, Huntsville, AL, January 16-18, 1978.

[19] Goldberg U.C., "Separated Flow Treatment with a New Turbulence Model," AIAA Journal, Vol. 24, No. 10, October 1986, pp. 1711-1713.

$$
W = \begin{pmatrix} \rho \\ \rho u \\ \rho v \\ \rho e \end{pmatrix}, \quad
F = \begin{pmatrix} \rho u \\ \rho u^2 - \sigma_{xx} \\ \rho uv - \tau_{xr} \\ \rho ue + \dot{q}_x - \sigma_{xx} u - \tau_{xr} v \end{pmatrix}, \quad
G = \begin{pmatrix} \rho v \\ \rho uv - \tau_{xr} \\ \rho v^2 - \sigma_{rr} \\ \rho ve + \dot{q}_r - \tau_{xr} u - \sigma_{rr} v \end{pmatrix}
$$

$$
H = \begin{pmatrix} 0 \\ 0 \\ -\sigma_+ \\ 0 \end{pmatrix}
$$

$$
\sigma_{xx} = -p - \frac{2}{3}(\mu + \mu_t)\nabla \cdot U + 2(\mu + \mu_t)\frac{\partial u}{\partial x} \tag{2}
$$

$$
\sigma_{rr} = -p - \frac{2}{3}(\mu + \mu_t)\nabla \cdot U + 2(\mu + \mu_t)\frac{\partial v}{\partial y} \tag{3}
$$

$$
\sigma_+ = -p - \frac{2}{3}(\mu + \mu_t)\nabla \cdot U + 2(\mu + \mu_t)\frac{v}{y}\alpha \tag{4}
$$

$$
\tau_{rx} = \tau_{xr} = (\mu + \mu_t)\left(\frac{\partial u}{\partial y} + \frac{\partial v}{\partial x}\right) \tag{5}
$$

$$
\dot{q}_x = -c_p\left(\frac{\mu}{\mathrm{Pr}} + \frac{\mu_t}{\mathrm{Pr}_t}\right)\frac{\partial T}{\partial x} \tag{6}
$$

$$
\dot{q}_r = -c_p\left(\frac{\mu}{\mathrm{Pr}} + \frac{\mu_t}{\mathrm{Pr}_t}\right)\frac{\partial T}{\partial y} \tag{7}
$$

$$
e = c_v T + \frac{1}{2}(u^2 + v^2) \tag{8}
$$

$$
\nabla \cdot U = \frac{\partial u}{\partial x} + \frac{\partial v}{\partial y} + \frac{v}{y}\alpha \tag{9}
$$

where $\alpha = 1$ for axisymmetric flow and 0 for two-dimensional flow.

In Equations 2-7, the laminar and eddy viscosities, μ and μ_t, are implicitly divided by the reference Reynolds number. The equations used for the Euler (inviscid) calculations are obtained from Equations 1-9 by setting both laminar and eddy viscosities to zero. The flow medium is assumed to be a perfect gas satisfying the equation of state,

$$
p = \rho \Re T \tag{10}
$$

The following power law was used to relate molecular viscosity to temperature: [20]

$$
\frac{\mu}{\mu_o} = \left(\frac{T}{T_o}\right)^n \tag{11}
$$

where $\mu_o = 0.1716$ mP, $T_o = 491.6$ R, and $n = 0.64874$. The laminar and turbulent Prandtl numbers, Pr and Pr_t, were assumed constant with values of 0.72 and 0.9 respectively. The ratio of specific heats, γ, was also assumed constant. The specific heat capacities at constant volume and pressure, c_v and c_p, are related as $\gamma = c_p/c_v$ and $\Re = (\gamma - 1)c_p/\gamma$.

[20] Mazor G., Ben-Dor G., and Igra O., "A Simple and Accurate Expression for the Viscosity of Nonpolar Diatomic Gases up to 10,000 K," AIAA Journal, Vol. 23, No. 4, April 1985, pp. 636-638.

Assuming a time-invariant grid and using the transformation of coordinates implied by $\tau = t, \xi = \xi(x,y), \eta = \eta(x,y)$, Equation 1 can be recast into conservation form where ξ and η are the new independent variables and x_ξ, x_η, y_ξ, and y_η are the four transformation coefficients obtained numerically from the mapping procedure.[8]

$$\frac{\partial W}{\partial \tau} + \frac{1}{\text{Area}} \left((y_\eta F - x_\eta G)_\xi + (-y_\xi F + x_\xi G)_\eta + \frac{G}{y} - \frac{H}{y} \right) = 0 \qquad (12)$$

The "Area" in Equation 12 denotes the area of the finite volume cell under consideration at the time of discretization of the equations. The transformed time variable is represented by τ.

2. Turbulence Modeling.

The shock/boundary-layer interference flowfield between projectile and launch tube as well as the projectile wake can include regions of recirculating flow. Modeling of these regions can be critical to the overall flowfield solution quality. However, most existing turbulence models either do not treat such regions or do so in a semi-empirical fashion that is frequently inadequate. To improve the predictive capability of separated flows using RANS codes a new turbulence model has been recently developed.[19] The new model is based on experimental observations of detached flows. The model prescribes turbulence kinetic energy (k) and dissipation (ϵ) analytically within backflows. A Gaussian variation of k normal to wall surfaces is assumed. The length scale of turbulence is proportional to the local distance from the wall to the edge of the viscous sublayer which is located outside the backflow region. The latter feature is a basic assumption of the model. The stress scale is the local maximum Reynolds stress which typically occurs around the middle of the boundary layer well outside the separation bubble. This scale must be supplied by a turbulence model that is used beyond backflow regions.

The main equations of the backflow model are given in Reference 19. A formula for the eddy viscosity (μ_t) distribution within backflows is derived and used for the RANS equations when the calculations are done inside separation bubbles. Outside of them, another turbulence model (for example Baldwin-Lomax[18]) supplies the values of eddy viscosity. While the Baldwin-Lomax turbulence model is used to detect flow separation and to initiate application of the backflow model, the latter model can relocate the separation point. Comparisons of the Baldwin-Lomax turbulence model and Goldberg's backflow model are given in References 10 and 21. For further details of how the model treats the influence of large eddies residing outside detached regions, the history effect of these eddies downstream of reattachment, and the mutual influence of multiple walls on the eddy viscosity, see References 19 and 22.

[21] *Goldberg, U.C., "Separated Flows Calculations With A New Turbulence Model," presented at the IACM First World Congress on Computational Mechanics, Austin, TX, Sept. 1986.*

[22] *Goldberg, U.C., "Prediction of Separated Flows With A New Turbulence Model," AIAA Journal, Vol. 26, No. 4, April 1988, pp. 405-408.*

3. Computational Algorithm.

The spatial discretization technique for the equations of motion (Equation 1) must be reliable and robust if it is to successfully capture the complex physics of projectile/launch tube interacting flowfields. The TVD formulation for the convective terms (the hyperbolic part of the time-dependent Navier-Stokes equations) along with a special treatment of the dissipative terms provides an appropriate simulation. In recent years, TVD formulations have been constructed for shock-capturing finite-difference methods.[8,9] Near large gradients in the solution (extrema) TVD schemes automatically reduce to first-order accurate discretizations locally while in general they can be constructed to be of higher-order accuracy. This local effect restricts the maximum global accuracy possible for TVD schemes to third order for steady-state solutions.

TVD methods manifest many properties desirable in numerical solution procedures. By design they avoid numerical oscillations and "expansion shocks" while at the same time being of higher-order accuracy; "expansion shocks" are shock waves which do not satisfy the entropy inequality. TVD formulations are also based on the principle of discrete or numerical conservation which is the numerical analog of physical conservation of mass, momentum, and energy. Thus, TVD schemes can "capture" flowfield discontinuities (e.g. shock waves) with high resolution. At a fundamental level they are based on upwind schemes; therefore, they closely simulate the signal propagation properties of hyperbolic equations. Schemes based on the TVD formulation are completely defined. In contrast, schemes based solely on central differences involve global dissipation terms for stability and have one or more coefficients that must be judiciously chosen to achieve desirable results.

Any conventional time discretization method suitable for the Navier-Stokes equations can be used together with this space discretization methodology; for example, approximate factorization and relaxation techniques. Proper treatment of the dissipative terms of the Navier-Stokes equations is also important in the construction of reliable numerical methods. Unidirectional second derivative terms are treated by using central difference approximations. Cross derivatives are represented by finite-differences the nature of which depends upon the sign of the coefficient of such terms. This treatment augments diagonal dominance of the resulting set of discretized equations without detracting from the accuracy and while adding to the reliability of the numerical procedure. Further details can be found in References 8 and 9.

4. Computational Grid.

Computing in-bore projectile flowfields is complicated by the multi-wall geometry. As illustrated in Figures 1 and 2 the ram accelerator projectile consists of several sharp corners that would severely hamper conventional grid generation schemes that require one set of grid lines to be tangent to surfaces and another set to be normal to them. This geometry is more easily gridded by the zonal approach. The internal geometry of the ram accelerator launch system in broken up into two zones of simple geometric shape (Figure 4). In each zone any approach to generating the grid can be used such as algebraic methods, differential equations methods, etc. In this case an algebraic grid is used with clustering near surfaces

and other regions in the flowfield where high gradients are expected (Figure 5). In the zonal approach, the computational method and computer program are constructed in such a manner that each zone may be considered as an independent module interacting with each other before or after the information corresponding to each zone is updated one cycle. In addition, the zonal boundaries are transparent to flowfield phenomena (e.g. shock waves). The actual grid used for these computations ($\simeq$ 30,000 nodes) consisted of the following dimensions for zones 1 and 2: 457x51, 201x21. The computational domain starts a small distance forward of the body and extends 1.5 projectile body lengths downstream. The computational results were found to be essentially independent of further grid refinement when all other factors were the same. A dense grid is preferred for resolving flow details within boundary layers, to prevent shock smearing, and to resolve shock/boundary-layer interactions. Grid zones have been generated in such a manner that the vertical families of mesh lines are continuous between zones 1 and 2 aft of the projectile. While this type of grid is natural for this problem the computational methodology permits a wider class of patched zonal grids where neither horizontal nor vertical grid lines need be continuous across zones.

5. Results.

Numerical simulations for non-reacting flow were performed using the four geometries listed with Figure 2. The diffuser area ratio is defined as,

$$\text{Diffuser Area Ratio} = \frac{(\text{tube diameter})^2}{(\text{tube diameter})^2 - (\text{max. projectile diameter})^2}$$

Small ratios indicate large clearance between projectile and tube walls. Calculations were performed on the BRL CRAY-2 supercomputer using 1.0 to 1.3 CPU hours per steady-state solution. Upstream boundary conditions are specified (slug flow) while supersonic outflow conditions are extrapolated. Numerical simulations were done in the projectile-fixed reference frame thus, a no-slip condition is employed on the projectile body while the tube wall translates at the freestream velocity. The plotted results have been transformed to the inertial reference frame.

Figure 6 shows the computed pressure contours for the 38mm configuration 1, velocity of 1102 m/s ($M = 3.022$), and tube fill pressure of 25 atm (Re = 2.3×10^8 based on body length). An oblique shock is attached to the nose of the projectile. This shock reflects from the tube wall and again from the turbulent boundary layer on the body. Multiple shock/boundary-layer interactions occur downstream. Contours in the wake show a weakening of shock reflections. The horizontal line extending from the projectile base downstream is the zonal grid boundary and is transparent to the flowfield. Figures 7 and 8 show the computed pressure contours for the 38mm configuration 2 for a velocity of 1102 m/s ($M = 3.022$) tube pressure 25atm, and 1430 m/s ($M = 3.95$) tube pressure 20atm, respectively.

Figure 9 shows the computed tube wall pressure for the 38mm configuration 2, $M = 3.022$ and tube fill pressure 25 atm. Computations for inviscid, laminar, and turbulent

flow are compared to pressures measured at the University of Washington (unpublished). Overall the comparison is quite good even in the wake region ($x \geq .17$m). The pressure rise between $.05 \leq x \leq .075$m, caused by the initial reflection of the body nose shock on the tube wall, is simulated but at a reduced magnitude (perhaps due to the steady flow assumption). Two pressure peaks between $.075 \leq x \leq .1$m are computed with the second slightly overpredicting the measured peak at $x \simeq .1$m. These peaks arise from secondary reflection of the body nose shock on the tube wall. The simulations produce noticeable but insignificant differences in wall pressure for inviscid, laminar, and turbulent modeling; however, projectile surface and tube centerline (wake) pressures are affected to a greater degree by boundary layer modeling as shown in Figures 10 and 11. Pressure oscillations on the body surface (Fig. 10, $0 \leq x \leq .07$m) are caused by pressure signals that travel upstream in the near-wall flowfield and may be related to the use of a body-fixed coordinate system. Figure 12 shows tube wall pressure distributions for both 38mm configurations. Although the general trends are the same, the pressure levels for configuration 2 are significantly larger. Configuration 2 has a 18% larger diffuser area ratio (i.e. smaller diffuser area resulting in higher pressures) and boundary layer thicknesses are different as well. Figure 13 shows tube wall pressure for $M = 3.022$ and 3.95. At the higher velocity the body nose shock intersects the tube wall farther downstream and causes shock reflections that result in lower pressures along the tube wall. Low Mach number ($M = 3.022$) simulations for configuration 2 produce a double pressure pulse at $x \simeq .1$m; this is caused by the intersection of a reflected shock from the tube wall near the end of the projectile forebody (see Figure 7). In the wake region ($x \geq .17$m) tube wall pressures are nearly invariant for these Mach numbers.

Figure 14 shows tube wall pressure comparisons for the 120mm configuration 2 using inviscid and turbulent flow and the same flow conditions as previous figures (Re = 9.7×10^8 based on body length). Inviscid flow modeling yields higher pressures downstream of initial and secondary shock reflections ($x \geq .3$m) but lower pressures in the wake region ($x \geq .54$m). Figure 15 shows the comparison of tube wall pressures for both configurations of the 120mm geometry. Configuration 2 shows slightly higher pressures than configuration 1 since the diffuser area is 15% larger. A similar comparison for the 38mm geometry (Figure 12) showed large differences in tube wall pressures. The projectile forebody and afterbody angles are similar for 120mm configurations but noticeably different for 38mm configurations. Figure 16 shows 120mm configuration 2 tube wall pressure for $M = 3.022$ and 3.95. At the higher velocity the body nose shock intersects the tube wall farther downstream but causes shock reflections that result in similar pressures along the tube wall. Figure 17 shows tube wall pressures for 38mm configuration 2 (compared to data in Fig. 9) and 120mm configurations 1 and 2 (x non-dimensionalized by the total body length, L). Due to different scales for the 38mm and 120mm geometries, Reynolds number effects are significant. Smaller differences in tube wall pressure for 38mm and 120mm geometries result from higher Mach number ($M = 3.95$) simulations as illustrated in Figure 18; however, large differences are apparent in the wake flow ($x/L \geq 1$) for both Mach number cases.

9

IV. REACTING FLOW

The BRL-LFD RAMCOMB (RAMjet COMBustion) code has been used for the numerical simulation of solid fuel combustion in a tubular solid-fuel ramjet (SFRJ) projectile.[11] Solid fuel regression rate and projectile thrust predictions compare favorably with in-flight and ground test data. For the SFRJ application the RAMCOMB code simulated a mass-controlled (stoichiometric) reaction of non-premixed solid fuel and oxygen using classical diffusion flame assumptions. A reaction rate expression was not required since the reaction was diffusion-controlled and the reactants were fully consumed and thus, could not coexist at any point in the flowfield. For application to the ram accelerator system the RAMCOMB code was modified for premixed, finite-rate, gaseous fuel combustion. Reaction rates are formulated in terms of temperature and species mass fraction. Reactants and products may coexist and need not be fully consumed in the reaction. RAMCOMB simulates subsonic flow and thus, reacting flow simulations are constrained to the flowfield downstream of the normal shock (Figure 3).

1. Equations of Motion.

The ram accelerator projectile configuration can support a region of low speed recirculating flow in the subsonic flowfield downstream of the normal shock (Figure 3). Thus the conservation equations are elliptic in form. Since the geometry is axisymmetric the equations can be written in cylindrical coordinates. The velocity components in this system are u, v, and w for the radial (r), azimuthal (θ), and axial (z) directions, respectively. Axisymmetric flow is assumed thus, all θ-derivatives are ignored; however, the azimuthal velocity component and the azimuthal momentum equation are retained. Since steady flows are considered, time derivatives ($\partial/\partial t$) are ignored. The conservation equations for mass (global) and momentum are given by,[23]

$$\nabla \cdot \rho \vec{V} = \frac{1}{r}\frac{\partial(r\rho u)}{\partial r} + \frac{\partial(\rho w)}{\partial z} = 0 \tag{13}$$

$$\nabla \cdot [\rho u \vec{V} - \vec{\tau_r}] - \frac{1}{r}[\rho v^2 - \tau_{\theta\theta}] + \frac{\partial p}{\partial r} = 0 \quad \text{(radial)} \tag{14}$$

$$\nabla \cdot [\rho w \vec{V} - \vec{\tau_z}] + \frac{\partial p}{\partial z} = 0 \quad \text{(axial)} \tag{15}$$

$$\frac{1}{r}\nabla \cdot [r(\rho v \vec{V} - \vec{\tau_\theta})] = 0 \quad \text{(azimuthal)} \tag{16}$$

Energy conservation for a compressible flow is expressed by the First Law of Thermodynamics. The steady form of the First Law states that the net rate of stagnation enthalpy (h) inflow for a control volume is equal to the sum of the shear work done by the contents of the control volume on the surroundings ($\vec{\tau}$) and the heat transfer to the surroundings.[23]

$$\nabla \cdot \left[\rho \vec{V} h + \vec{J_h} + \sum_j h_j \vec{J_j} + \vec{J_k} - (u\vec{\tau_r} + v\vec{\tau_\theta} + w\vec{\tau_z})\right] = 0 \tag{17}$$

---

[23] Schlichting, H., Boundary Layer Theory, 7th ed., translated by J. Kestin, McGraw-Hill, New York, 1979.

where mass, heat, and turbulence kinetic energy flux are defined as,

$$\vec{J}_j = (\mu_{\text{eff}}/\text{Re})\nabla m_j = \Gamma_j \nabla m_j$$
$$\vec{J}_h = (\mu_{\text{eff}}/\text{Pr})c_{p_j}\nabla T = \Gamma_h c_{p_j} \nabla T$$
$$\vec{J}_k = (\mu_{\text{eff}}/\text{Pr})\nabla k = \Gamma_k \nabla k$$

The mass fraction and molar specific enthalpy for species j are m_j and h_j, respectively. Radiation flux is neglected in Equation 17, but will be explored in future reports.

In Equations 14-17 the shear stress (τ) includes the Reynolds stress with an effective fluid viscosity expressed as the sum of the molecular and turbulent viscosities, $\mu_{\text{eff}} = \mu + \mu_t$. The subscript "eff" serves as a reminder that the turbulent fluid properties are being treated as kinematic properties with a set of augmented transport coefficients. The calorically perfect gas assumption is made since the temperature dependence of c_{p_j} for the reactants and products is not well determined. The Prandtl number (Pr) is assumed to be nearly unity (.9) which is considered adequate for gaseous flows even with combustion[24].

For flows that are subsonic and dominated by recirculation the stream function-vorticity form of the governing equations has been widely utilized.[23] This form facilitates the use of numerically efficient Gauss-Seidel relaxation algorithms. Stream function, ψ, and vorticity, ω are defined using,[23]

$$\frac{\partial \psi}{\partial r} = r\rho w \qquad (18)$$

$$\frac{\partial \psi}{\partial z} = -r\rho u \qquad (19)$$

$$\omega = \nabla \times \vec{V} = \left[\frac{\partial u}{\partial z} - \frac{\partial w}{\partial r}\right] = -\left[\frac{\partial}{\partial z}\left(\frac{1}{r\rho}\frac{\partial \psi}{\partial z}\right) + \frac{\partial}{\partial r}\left(\frac{1}{r\rho}\frac{\partial \psi}{\partial r}\right)\right] \qquad (20)$$

The governing equations are derived in Reference 11 and can be expressed in the form of a general variable ϕ. This variable can represent stream-function, vorticity, azimuthal velocity, stagnation enthalpy, or species mass fraction.

$$a_\phi\left[\frac{\partial}{\partial z}\left(\phi\frac{\partial \psi}{\partial r}\right) - \frac{\partial}{\partial r}\left(\phi\frac{\partial \psi}{\partial z}\right)\right] - \frac{\partial}{\partial z}\left[b_\phi r \frac{\partial}{\partial z}(c_\phi\phi)\right] - \frac{\partial}{\partial r}\left[b_\phi r \frac{\partial}{\partial r}(c_\phi\phi)\right] + rd_\phi = 0 \qquad (21)$$

$\phi = \psi, \qquad a_\phi = 0, \qquad b_\phi = 1/(\rho r^2), \qquad c_\phi = 1, \qquad d_\phi = -\omega/r$

$\phi = \omega/r, \qquad a_\phi = r^2, \qquad b_\phi = r^2, \qquad c_\phi = \mu_{\text{eff}}, \qquad d_\phi = Q_\omega$

$\phi = rv, \qquad a_\phi = 1, \qquad b_\phi = \mu_{\text{eff}}r^2, \qquad c_\phi = 1/r^2, \qquad d_\phi = 0$

$\phi = \tilde{h}, \qquad a_\phi = 1, \qquad b_\phi = (\Gamma_h)_{\text{eff}}, \qquad c_\phi = 1, \qquad d_\phi = Q_h - S_h$

$\phi = m_j, \qquad a_\phi = 1, \qquad b_\phi = (\Gamma_j)_{\text{eff}}, \qquad c_\phi = 1, \qquad d_\phi = -R_j$

$$Q_\omega = -\frac{\partial}{\partial z}(\rho v^2) - r\left[\frac{\partial}{\partial z}\left(\frac{u^2+w^2}{2}\right)\frac{\partial \rho}{\partial r} - \frac{\partial}{\partial r}\left(\frac{u^2+w^2}{2}\right)\frac{\partial \rho}{\partial z}\right] - r^2 S_\omega$$

[24] Bradshaw, P., Cebeci, T., and Whitelaw, J.H., *Engineering Calculation Methods for Turbulent Flows*, Academic Press, New York, 1981.

$$Q_h = \frac{1}{r}\frac{\partial}{\partial z}\left[\mu_{\text{eff}} r\left(\left(1-\frac{1}{\sigma_h}\right)\frac{\partial(V^2/2)}{\partial z} + \left(\frac{1}{\sigma_k}-\frac{1}{\sigma_h}\right)\frac{\partial k}{\partial z} + \sum_j\left(\frac{1}{\sigma_j}-\frac{1}{\sigma_h}\right)h_j\frac{\partial m_j}{\partial z}\right)\right]$$

$$S_h = \frac{1}{r}\frac{\partial}{\partial r}\left[\mu_{\text{eff}} r\left(\left(1-\frac{1}{\sigma_h}\right)\frac{\partial(V^2/2)}{\partial r} + \left(\frac{1}{\sigma_k}-\frac{1}{\sigma_h}\right)\frac{\partial k}{\partial r} + \sum_j\left(\frac{1}{\sigma_j}-\frac{1}{\sigma_h}\right)h_j\frac{\partial m_j}{\partial r}\right)\right]$$

S_ω is defined in Reference 11.

σ $= \mu_{\text{eff}}/\Gamma$

R_j = reaction rate per unit volume for species j.

For N species only $N-1$ specie equations ($\phi = m_j$) must be solved, since the sum of the mass fractions must equal unity. In effect the continuity equation (Eq. 13) is the Nth specie equation since the summation of all specie equations yields the continuity equation. The mixture equation of state follows from Dalton's Law,

$$p = \rho\bar{\Re}T\sum_j\frac{m_j}{\mathcal{M}_j} \tag{22}$$

where $\bar{\Re} = \Re\sum_j\mathcal{M}_j$, $\mathcal{M}_j$ is the molecular weight of species j, and $\Re$ is the specific gas constant. Mixture temperature (T) is obtained from the conservation of energy expressed in terms of the stagnation enthalpy,

$$\tilde{h} = T\sum_j c_{p_j}m_j + \left[1-\frac{1}{\Pr}\right]\frac{V^2}{2} + \left[\frac{1}{\text{Sc}}-\frac{1}{\Pr}\right]\frac{\tilde{V}^2}{2} + \left[\frac{1}{\text{Sc}}-\frac{1}{\Pr}\right]\sum_j h_j m_j \tag{23}$$

with $V = (u^2+v^2+w^2)^{1/2}$, and $\tilde{V}$ is the magnitude of the turbulent (fluctuating) velocity. The Schmidt number (Sc) is assumed to be unity. Mixture viscosity (μ) is defined using Sutherland's expression[25] for $T \leq 3400R$ and using Equation 11 for higher temperatures.

$$\mu = 2.270\text{x}10^{-8}\frac{T^{1.5}}{T+198.6} \tag{24}$$

2. Turbulence Modeling.

A two-equation turbulence model suggested by Kim and Chung[26] for reacting flows has been added to the code. This model describes the turbulence viscosity (μ_t) as a function of turbulence kinetic energy (k) and dissipation rate (ϵ) variables. A set of partial differential equations is written for k and ϵ and solved along with the Navier-Stokes equations (Equation 21).

$$\rho w\frac{\partial k}{\partial z} + \rho u\frac{\partial k}{\partial r} - \frac{1}{r}\left[\frac{\partial}{\partial z}\left(r\mu_k\frac{\partial k}{\partial z}\right) + \frac{\partial}{\partial r}\left(r\mu_k\frac{\partial k}{\partial r}\right)\right] = G - \rho\epsilon \tag{25}$$

[25] Ames Research Staff, "Equations, Tables, and Charts for Compressible Flow," NACA Report 1135. 1956.

[26] Kim, Y.M., and Chung, T.J., "Finite-Element Analysis of Turbulent Diffusion Flames," AIAA Journal, Vol. 27. No. 3. March 1989. pp. 330-339.

$$\rho w \frac{\partial \epsilon}{\partial z} + \rho u \frac{\partial \epsilon}{\partial r} - \frac{1}{r} \left[\frac{\partial}{\partial z} \left(r \mu_\epsilon \frac{\partial \epsilon}{\partial z} \right) + \frac{\partial}{\partial r} \left(r \mu_\epsilon \frac{\partial \epsilon}{\partial r} \right) \right] = \frac{C_1 G \epsilon}{k} - \frac{C_2 \rho \epsilon^2}{k} \qquad (26)$$

$$\mu_t = \frac{\rho C_3 k^2}{\epsilon} \qquad (27)$$

$$G = \mu_t \left[2 \left(\left(\frac{\partial w}{\partial z} \right)^2 + \left(\frac{\partial u}{\partial r} \right)^2 + \left(\frac{u}{r} \right)^2 \right) + \left(\frac{\partial w}{\partial r} + \frac{\partial u}{\partial z} \right)^2 \right] \qquad (28)$$

where, $\mu_k = \mu + \mu_t/\lambda_k, \mu_\epsilon = \mu + \mu_t/\lambda_\epsilon, \lambda_k = 1, \lambda_\epsilon = 1.3, C_1 = 1.44, C_2 = 1.92, C_3 = .09$. Results using this turbulence model will included in future reports.

3. Combustion Modeling.

Systems of chemical reactions are usually complex. A hydrocarbon fuel, for example, may contain hundreds of distinct chemical species. During combustion numerous short-lived intermediate species are formed in addition to the final products that include H_2O, CO, and CO_2. Inclusion of intermediate species and reaction steps within the framework of a calculation could be defeated by an ignorance of the thermodynamic, transport, and chemical-kinetic properties of these species. It is possible to make useful predictions of combustion processes by confining attention to a postulated global reaction between fuel and oxidizer that neglects intermediate steps.
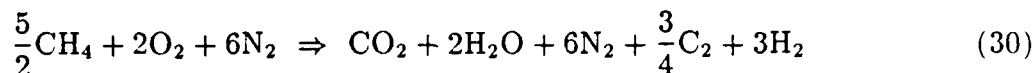
$$\text{Fuel} + \delta \text{Oxidizer} + \text{Diluents} \Rightarrow (1 + \delta)\text{Products} + \text{Diluents} \qquad (29)$$
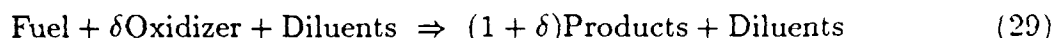
where δ is the stoichiometric oxidizer/fuel ratio. Two limitations of a global reaction model should be noted.[27] During the ignition delay period, when the complete reaction mechanism will predict the gradual buildup of free radicals with little or no perceptible temperature change, a global model will indicate an immediate exothermic (or endothermic) reaction with resulting temperature increase (or decrease). Secondly, the adiabatic flame temperature predicted by the global model will be higher than for the complete multi-step reaction mechanism. This results from the fact that a global model does not include all of the product species actually present in the reaction. If very low pressures are avoided, the discrepancy in flame temperature will not be significant.

Many of the assumptions commonly made in combustion models[28-30] are also incorporated into the present model; in particular, assumptions made in the *Shvab-Zeldovich* formulation.[30] The reacting fluid is treated as a continuum with equal mass diffusivity properties for all species. The specific heat at constant pressure (c_{p_j}) of each species is assumed constant in the gas phase (see Equation 23). The contribution of turbulence is included as turbulence kinetic energy (Equation 21, $\phi = k$) and the fluctuating velocity component ($\tilde{V}$) in Equation 23. A one-step, irreversible, temperature and mass controlled, finite-rate reaction is considered for which the reactant species need not be fully consumed. The reactants are gaseous fuel (CH_4) and oxidizer (O_2) premixed to stoichiometric proportions. The products of this reaction (e.g. CO_2 and H_2O) are lumped into one specie

---

[27] *Rogers, R.C., and Chinitz, W., "Using a Global Hydrogen-Air Combustion Model in Turbulent Reactin; Flow Calculations," AIAA Journal, Vol. 21, No. 4, April 1983, pp. 586-592.*

with averaged thermodynamic properties ($\mathcal{M}$ determined by a weighted average). Diluent species are included in Equations 22 and 23.

Hydrocarbon reactions are commonly used for ram accelerator testing at the University of Washington,[1] for example,

$$\frac{5}{2}CH_4 + 2O_2 + 6N_2 \Rightarrow CO_2 + 2H_2O + 6N_2 + \frac{3}{4}C_2 + 3H_2 \qquad (30)$$

This reaction is one of a general class of hydrocarbon reactions investigated by Westbrook and Dryer,[31]

$$C_aH_bO_c + \frac{1}{2}(a + \frac{b}{2} + c)O_2 \Rightarrow aCO + \frac{b}{2}H_2O \qquad (31)$$
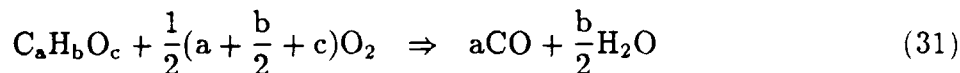
where elemental and diluent species N_2, C_2 and H_2 are ignored thus,

$$CH_4 + 2O_2 \Rightarrow CO_2 + 2H_2O \qquad (32)$$

CH_4 is considered the fuel, O_2 the oxidizer, and products are CO_2 and H_2O. Thermodynamic data is given in Table 1.

Table 1. Thermodynamic Data

	$c_p(\frac{cal}{mole\ K})$	$\Delta H_f^o(\frac{cal}{mole})$	$\mathcal{M}$
CH_4	8.536	-17895	16.043
O_2	7.017	0	32.000
CO_2	8.874	-94054	44.011
H_2O	8.025	-57798	18.016
Fuel	8.536	-17895	16.043
Oxidizer	7.017	0	32.000
Product	8.450	-75926	26.681

Elemental species (O_2, N_2, C_2, H_2) do not contribute to the heat of reaction since $\Delta H_f^o = 0$ but are included in the equations of state (Equations 22 and 23). The reaction is exothermic with a heat of reaction given by,[29]

$$\Delta H_r = \left(\sum_j n_j \Delta H_{f_j}^o\right)_{prod} - \left(\sum_j n_j \Delta H_{f_j}^o\right)_{reac} \qquad (33)$$

where n_j is the stoichiometric coefficient and $\Delta H_{f_j}^o$ is the heat of formation for each species j in Equation 30. For this reaction $\Delta H_r = $ -690224.8 J. For a methane/oxygen mixture

[28] Khalil, E.E., Spalding, D.B., and Whitelaw, J.H., "The Calculation of Local Flow Properties in Two-Dimensional Furnaces," International Journal of Heat and Mass Transfer, 1975, Vol. 18, pp. 775-791.

[29] Kuo, K.K., Principles of Combustion, John Wiley and Sons, Inc., New York, 1986.

[30] Williams, F.A., Combustion Theory, Addison-Wesley Publishing Company, Inc., 1965.

[31] Westbrook, C.K., and Dryer, F.L., "Chemical Kinetic Modeling of Hydrocarbon Combustion," Progress in Energy Combustion Science, Vol. 10, pp. 1-57.

at 300°K, the heat of reaction is nearly invariant with pressure above 10 atm.[32] The combustion flame temperature is given by,[29]

$$\Delta H_r + \left(\sum_j n_j (h_{T_f} - h_{T_i})_j \right)_{\text{prod}} = 0 \tag{34}$$

where T_f is the adiabatic frozen-flame temperature and T_i is the initial or base-state temperature (e.g. 298K). For the particular reaction (Equation 30) T_f can be iteratively computed to be 1643.06K (2957.50R).

Conservation of chemical species can be written for each specie in Equation 32. For example, the conservation of mass for product CO_2 is given by (see Equation 21, $\phi = m_{CO_2}$),

$$\frac{\partial}{\partial z}\left[m_{CO_2} \frac{\partial \psi}{\partial r} \right] - \frac{\partial}{\partial r}\left[m_{CO_2} \frac{\partial \psi}{\partial z} \right] - \frac{\partial}{\partial z}\left[(\Gamma_{CO_2})_{\text{eff}} r \frac{\partial m_{CO_2}}{\partial z} \right] - \frac{\partial}{\partial r}\left[(\Gamma_{CO_2})_{\text{eff}} r \frac{\partial m_{CO_2}}{\partial r} \right] - r R_{CO_2} = 0 \tag{35}$$

where Γ is a diffusion coefficient ($\mu_{\text{eff}}/\text{Re}$) and R_{CO_2} is the reaction rate per unit volume. The reaction rate is defined using the Law of Mass Action,*

$$R = C \prod_1^N m_j^{n_j} \tag{36}$$

where C is the specific reaction rate constant and $N = 4$ for Equation 32. Using an Arrhenius expression for C the reaction rate is approximated,[31]

$$R = A T^\alpha \exp\left(\frac{-E_a}{\Re T} \right) m_{CH_4}^a m_{C_2}^b \tag{37}$$

where $A T^\alpha$ is the collision frequency, the exponential term is the Boltzmann factor, and E_a is the activation energy. For the general hydrocarbon reaction, Reference 31 specifies $A = 8.3\text{x}10^5$ moles/cm^3-sec, $\alpha = 0$, $E_a = 125520$ J/mole, $a = -.3$, $b = 1.3$, and $\Re = 8.314$ J/K-mole. The magnitude of the collision frequency determines the speed at which the reaction progresses.

4. Computational Algorithm.

Equation 21 can be reduced to a successive-substitution formula for flow variable ϕ at each node on the computational grid. Central finite differences are used for the diffusive and source terms and upwind differences for the convective terms. Using upwind differencing in the specie conservation equations reduces the occurrence of negative specie mass fractions in mixing layers. The resulting system of equations for the entire grid is solved using a Gauss-Seidel relaxation scheme.[11] Each iteration cycle is made up of λ sub-cycles, where λ is the number of equations being considered (λ must be at least 2 since the equations for $\phi = \omega/r$ and $\phi = \psi$ are the minimum required to define the flow). In

---

[32] Kivity, Y., Grimberg, M., and Halevy, D., "Performance of the Ram Accelerator in the Oblique Detonation Mode," Proceedings of the 41st Meeting of the Aeroballistic Range Association, San Diego, CA, Oct. 22-25, 1990.

* "The rate of disappearance of a chemical species is proportional to the products of the concentrations of the reacting chemical species, each concentration being raised to a power equal to the corresponding stoichiometric coefficient"[29]

each sub-cycle grid points are scanned row by row and a single variable is updated. The variables ω/r and ψ are updated in order followed by all other variables. When all sub-cycles are completed a new iteration cycle is started in which the values of the variables from the latest iteration are immediately used. This is consistent with the Gauss-Seidel methodology.[33]   Convergence is satisfied when the greatest relative change in any flow variable, ϕ, over all grid points is smaller than a prescribed tolerance.

5. Results.

Reacting flow simulations were performed for two geometries, the 38mm configuration 2 and the 120mm configuration 2 (see Figure 2). The reaction considered is given by Equation 30 and the flow conditions were 1430 m/s velocity, 20 atm pressure and M = 3.95. For numerical simulations the mixture is assumed to have been ignited and a sustained reaction is taking place; comparisons between numerical and experimental data are only performed for cases where the projectile is sufficiently upstream of the ignition point. Simulation of mixture ignition will be included in future reports. The global reaction model should not be expected to reproduce exact profiles of chemical species nor should it necessarily model the ignition phase. Rather, the results obtained with the global model should be representative of the overall flowfield with regard to the mixing of the fuel and the overall heat release. Therefore, the parameters chosen for comparison should be static temperature, pressure, distribution of mixing and heat release.

The computational domain for reacting flow simulations extends from the subsonic flow upstream boundary (formed by the normal shock) that is usually positioned on the projectile body (Figure 3) to a far-field downstream boundary which is also assumed to be subsonic. For the thermally choked mode the downstream boundary eventually becomes sonic; however, the computational domain was not extended to this point. The upstream flow profiles are supplied from supersonic non-reacting flow computations (USA-PG code) while downstream conditions are extrapolated. Simulations are performed in the projectile-fixed reference frame (i.e. moving tube wall) and subsequently transformed to the inertial frame. Reacting flow simulations are performed for laminar flow modeling (i.e. $\mu_t = 0$) while results for reacting/turbulent flow will be included in future reports.

The two codes – USA-PG and BRL-LFD RAMCOMB – can be used in either an iterative fashion to obtain the supersonic/subsonic, inert/reacting flowfield or in a single sweep computation where the flowfield is partioned by a normal shock of known location. The former method has been used with success for a similar mixed flow problem.[11] In the latter method the supersonic/inert flow is computed using the USA-PG code which supplies flow profiles for subsonic/reacting computations using RAMCOMB after the normal shock is imposed. As an initial test of the codes the single sweep method was used for results in the present report using normal shock locations derived from data reported by the University of Washington.[1]

The computational grid for the 38mm configuration 2 starts .1074m (64% body length) from the projectile nose (i.e. the measured normal shock position) and ends .7m down-

---

[33] Carnahan, B., Luther, H.A., and Wilkes, J.O., Applied Numerical Methods, John Wiley and Sons, New York, 1969.

16

stream. In the streamwise direction 201 points are distributed and 51 points are used between the body and the launch tube wall. For the 120mm configuration 2 the same grid dimensions are distributed from .3441m from the projectile nose (assumed normal shock location, 64% body length) to 1.7m downstream. Calculations were performed on the US Army TACOM and US Army BRL CRAY-2 supercomputers in about .25 CPU hours per case.

Figure 19 shows computed and measured launch tube wall pressures for the 38mm configuration 2. Measured data show an apparent normal shock at .1074m. Flow upstream of the normal shock was computed using USA-PG and agreement with data is very good. This indicates that the inert and reacting flow may be partitioned. Downstream flow was computed using RAMCOMB and agreement with data is fair. A second pressure rise after the normal shock ($x \simeq .2$m) is not reproduced by the simulation indicating that the reaction zone may be spread over a larger distance than represented by the global one-step reaction with Arrhenius rate terms (see comments in section IV.3). In addition, the measurements were made for a projectile with bore-riding fins. The location of these fins with respect to the launch tube wall pressure transducer is not precisely known (i.e. the projectile rotates in the tube). Thus, measurements shown in Figure 19 may represent a tube wall/fin interaction. Further investigation is warranted. The computed and measured pressures show a decreasing trend downstream of the body ($x \geq .17$m) toward a sonic condition, characteristic of subsonic combustion.

Figure 20 shows a comparison between computed 38mm and 120mm geometry tube wall pressures for reacting flow. Streamwise distance has been nondimensionalized by the respective body lengths. The location of the normal shock was assumed to be at the same location (relative to total body length) for both geometries. Note that the inert flow pressures ($x/L \leq .64$) are very similar; this result consistent with that of Figure 18. The level of pressure in the reaction zone is smaller for the 120mm geometry.

Figure 21 shows a comparison between computed 38mm and 120mm geometry body wall pressures for reacting flow. No measurements have been reported on the projectile body to date. Pressure oscillations on the body surface ($0 \leq x \leq .15$m) are caused by pressure signals that travel upstream in the near-wall flowfield and may be related to the use of a body-fixed coordinate system. Pressures are similar for both geometries except for a pressure rise at $x/L \simeq .6$ and smaller pressures in the reaction zone for the 120mm geometry. Integration of these pressures yields a thrust coefficient ($T/P_\infty A$) of 1.48 for the 38mm geometry and 1.26 for the 120mm geometry. The reference quantities are tube fill pressure (P_∞) and tube cross-sectional area (A). For a similar fuel mixture in the 38mm system, Reference 5 reports a thrust coefficient of 2.3. In dimensional form the computed thrust (T) is 3400N and 28700N for the 38mm and 120mm geometries, respectively.

Figure 22 shows reaction rate contours for the 38mm configuration 2. The dashed line at $y = .019$m represents the launch tube wall while other dashed lines represent the boattail-base body geometry; recall that the calculation is started at $x = .1074$m from the projectile nose. Note that the figure is plotted with a skewed scale in order to include a larger flowfield area around the body thus, body angles are exaggerated. The clustering of contour lines near the imposed normal shock ($x = .1074$m) as well as tube and body walls (i.e. boundary layers) indicates large reaction rate gradients at these locations. The

17

magnitude of the reaction rate is also largest in these regions. Flow heating in these regions is the primary reason for increased reaction. Rate gradients are reduced in the projectile wake where reaction products accumulate reducing the magnitude of the reaction rate (see Equation 37) as shown in Figure 23. These simulations indicate that a larger percentage of the reaction (and thus high pressure) occurs on the afterbody as opposed to the projectile base. Thus, the widely used schematic shown in Figure 3 should be revised.

V. CONCLUSIONS AND FUTURE WORK

Computational fluid dynamics solutions of the Navier-Stokes equations have been applied to both non-reacting and reacting in-bore flowfields for a thermally choked ram accelerator projectile launch system. Separate computational fluid dynamics codes for inert flow (perfect gas) and reacting flow (finite-rate chemistry) were employed. The codes were used in an uncoupled fashion (i.e. specified normal shock location) to simulate the entire flowfield. Good comparison between computed and measured pressures for non-reacting flow in a 38mm system were achieved including the investigation of viscous modeling and geometric scaling to a 120mm system. Good comparison was also achieved between computed and measured pressures in the subsonic reaction zone.

Solutions that employ a coupling technique with USA-PG and BRL-LFD RAMCOMB are in progress and will reported at a future date. These solutions will be used to predict (and compare with measured data) projectile thrust derived from a variety of ram accelerator fuel/oxidizer mixtures and projectile velocities. Tests conducted at the University of Washington[5] have shown that thrust decreases with velocity, reaching a minimum near the Chapman-Jouguet detonation speed, and then showing an increasing trend. Numerical simulations will attempt to duplicate this trend. Investigation into the effects of turbulence modeling for reacting flows, alternative reaction rate expressions, and global versus multi-step reaction mechanisms is warranted. Parametric studies of initial gas mixture and pressure, projectile velocity and geometry (38mm and 120mm scales) and other effects are also planned.

The use of a fully coupled single-code CFD capability is also underway at the BRL using the latest versions of the USA-series codes. These codes include both equilibrium chemistry and finite-rate chemistry fully coupled to the gasdynamics and are capable of time-accurate simulations. The USA-series code will also be used to investigate the oblique detonation and superdetonative stages of ram accelerator operation. In these stages a mixed-mode flow is not involved since combustion occurs primarily in supersonic flow. Certain aspects of numerical simulations will therefore be greatly simplified. Three-dimensional simulations are planned and will include the bore-riding fins and effects of projectile balloting in the launch tube.
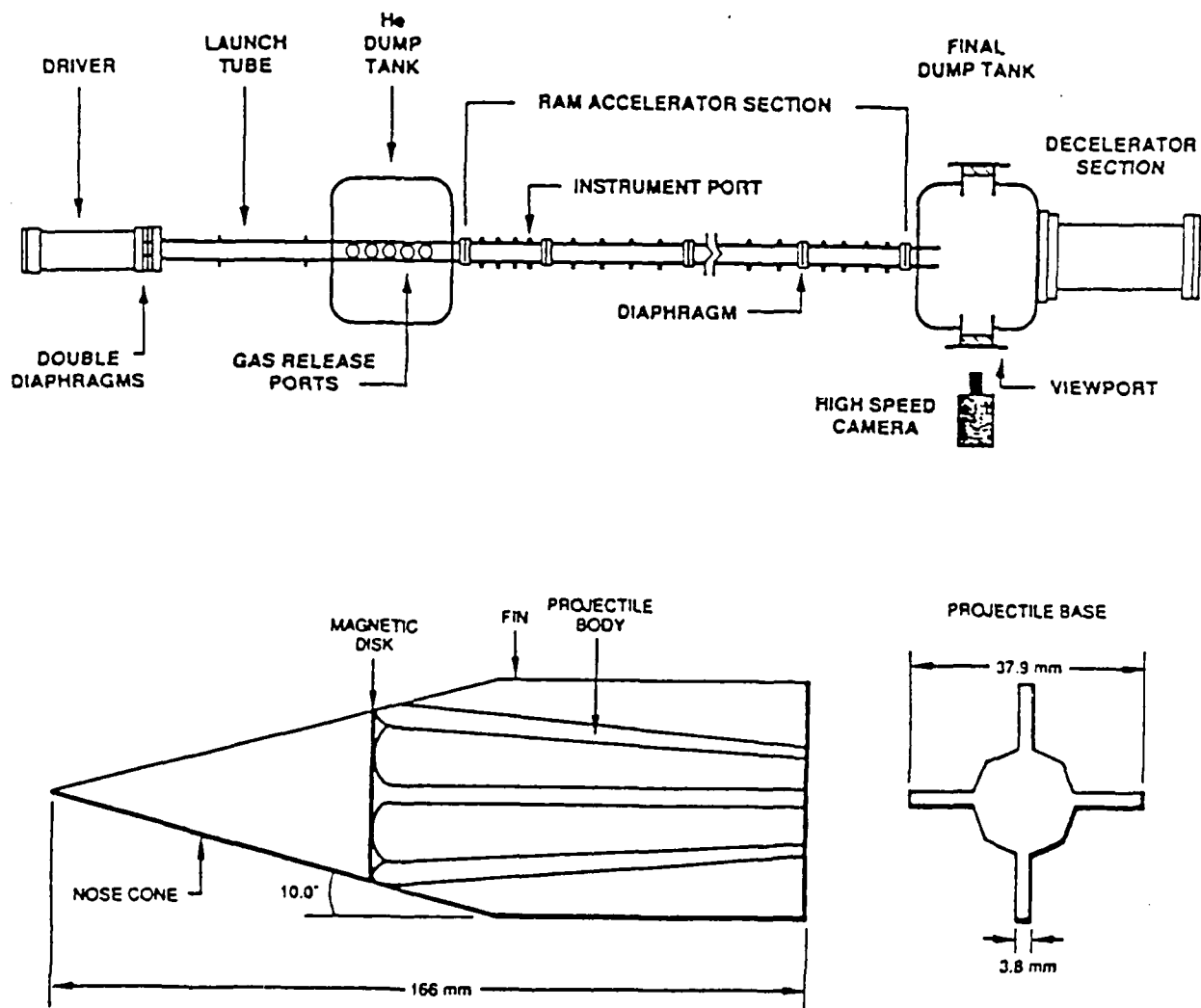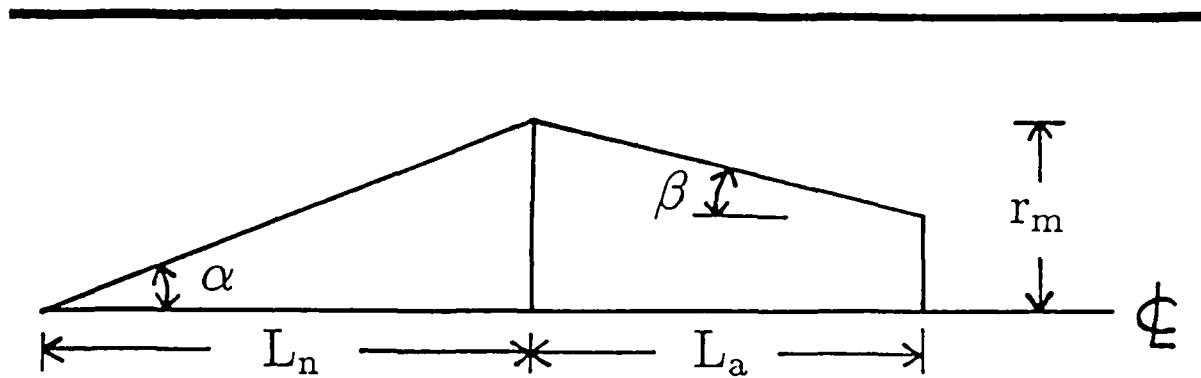
Figure 1. University of Washington Ram Accelerator facility and typical 38mm projectile.

Geometry	L_n	L_a	r_m	α	β	Diffuser Area Ratio
38mm Tube						
Config. 1	.06518	.06182	.0145	12.5	5.42	2.37
Config. 2	.08644	.08382	.0152	10.0	4.30	2.80
120mm Tube						
Config. 1	.26100	.26100	.0460	10.0	4.30	2.43
Config. 2	.27294	.26467	.0480	10.0	4.30	2.81

Figure 2. Ram Accelerator in-bore projectile geometry (excluding bore-rider fins); lengths in meters, angles in degrees.
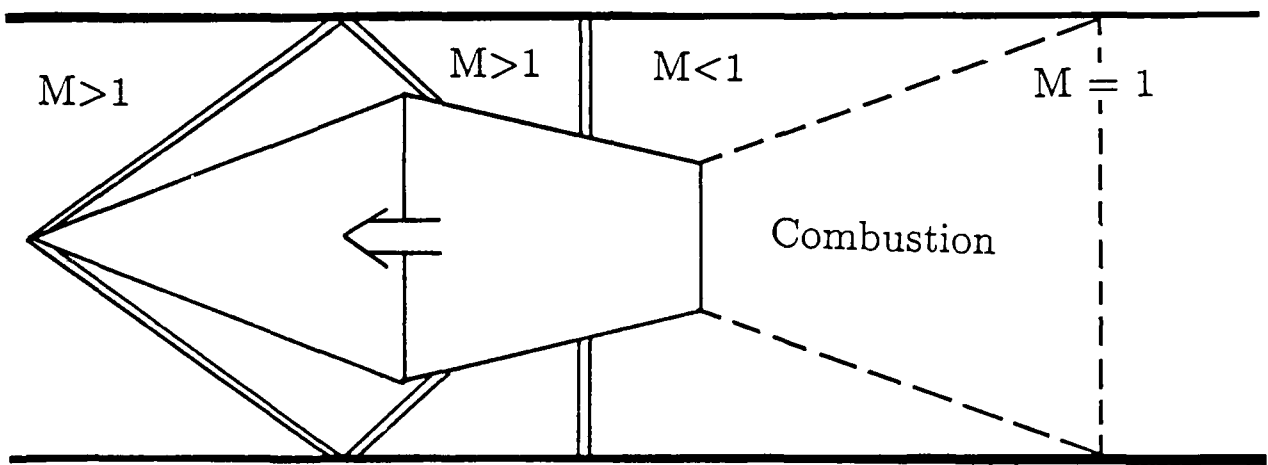
Figure 3. Schematic of Ram Accelerator in-bore flowfield; thermally choked mode.
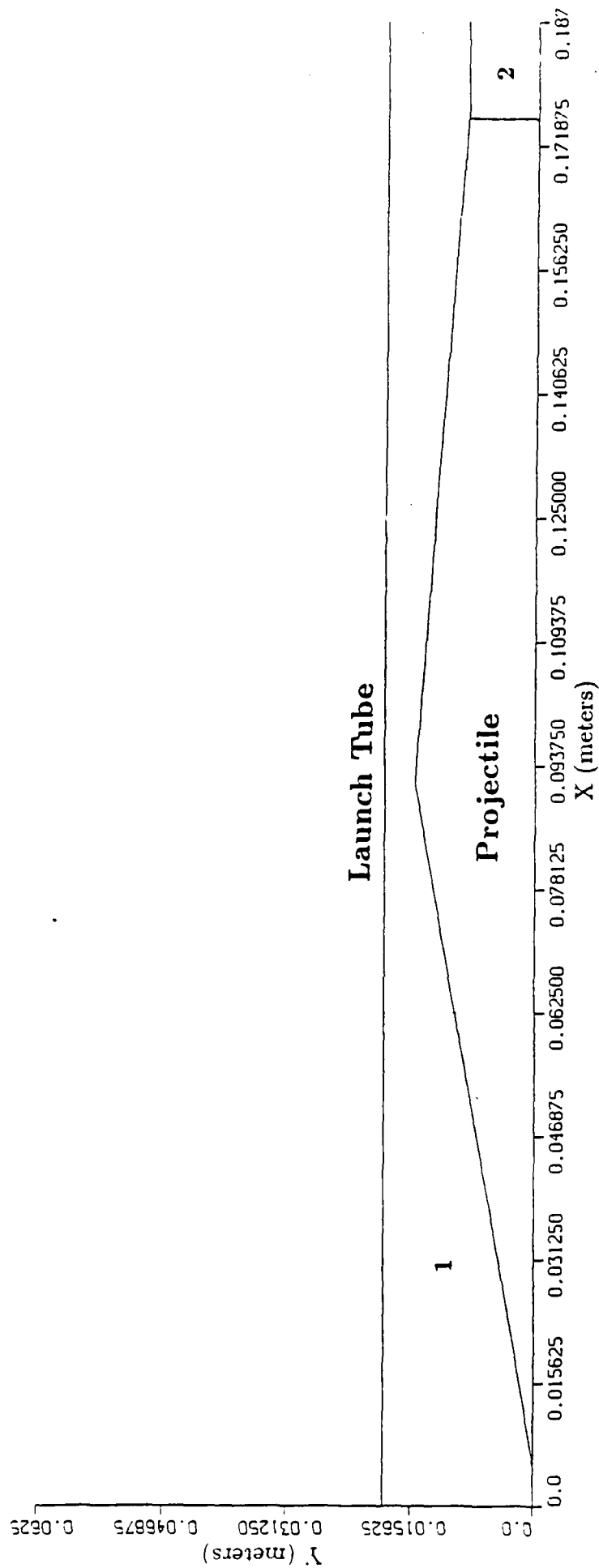
Figure 4. Zone designations for computational grid.
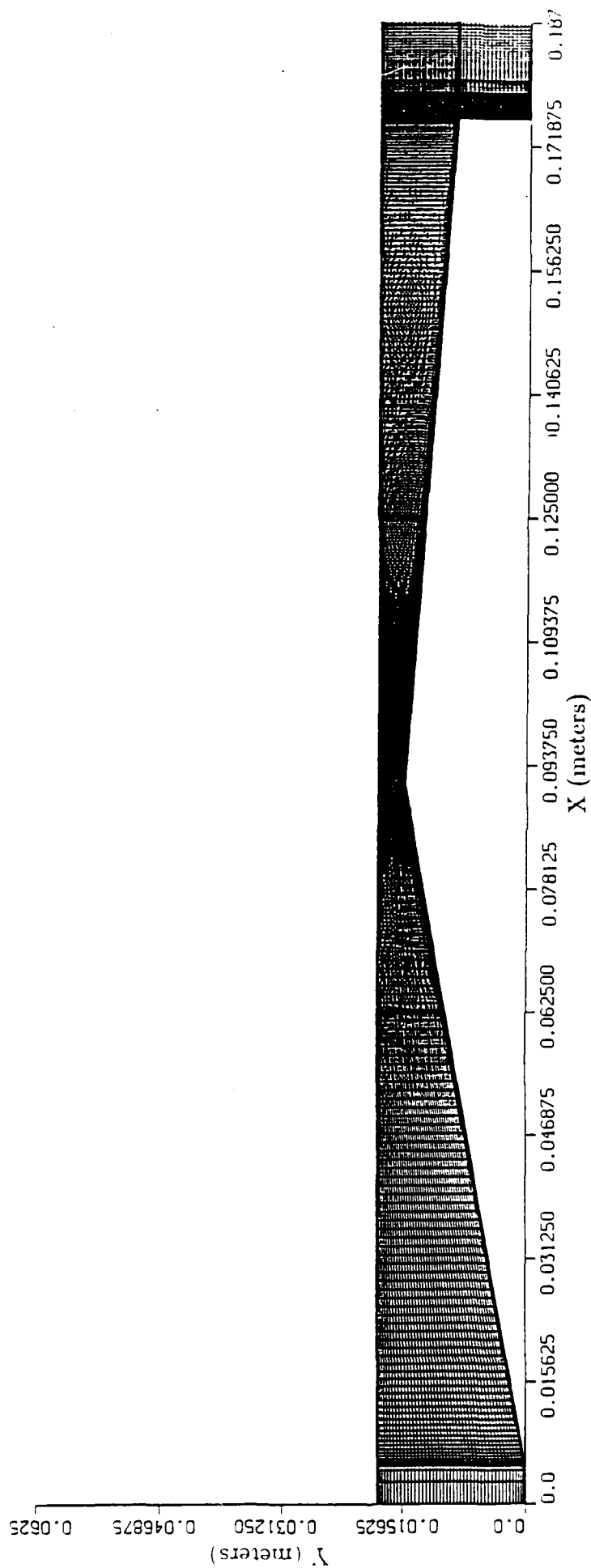
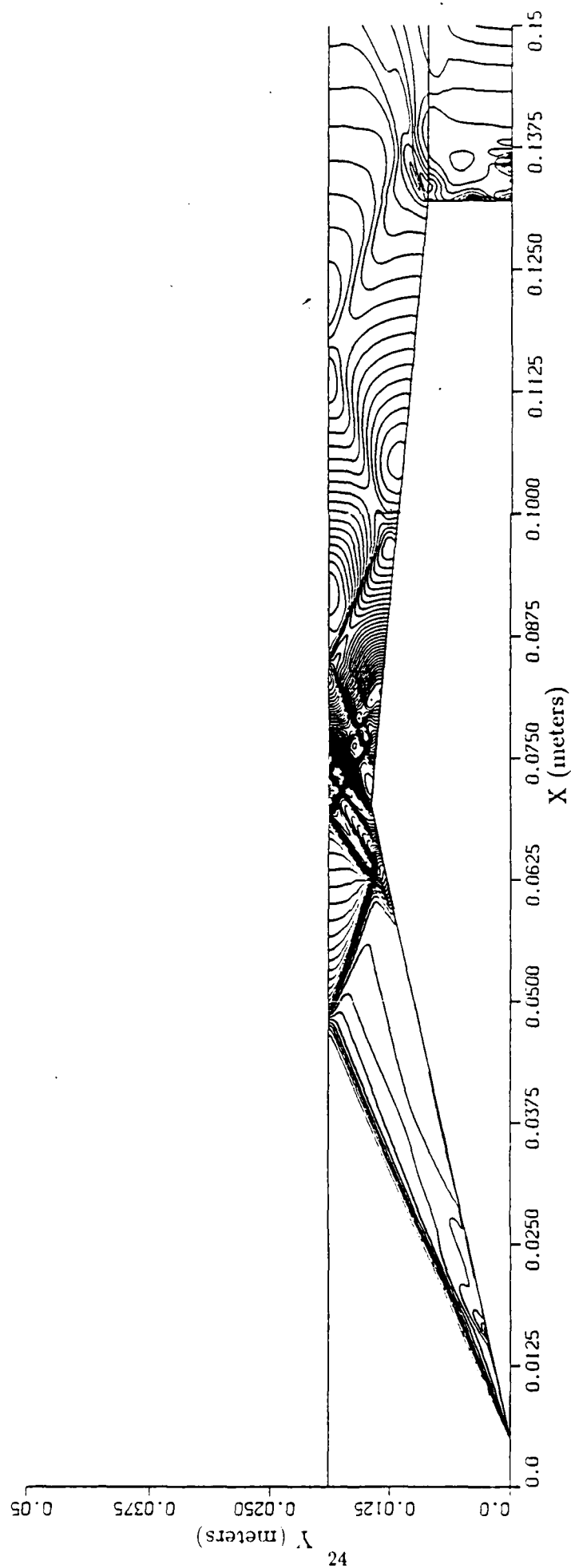**Figure 5.** Computational grid for typical Ram Accelerator and launch tube geometry (near-field shown).

23

Figure 6. Computed pressure contours for non-reacting turbulent flow, 38mm Config. 1, $M_\infty = 3.022, U_\infty = 1102\text{m/s}, P_\infty = 25\text{atm}, (.2 \leq P/P_\infty \leq 12, \Delta P = .1)$.

24

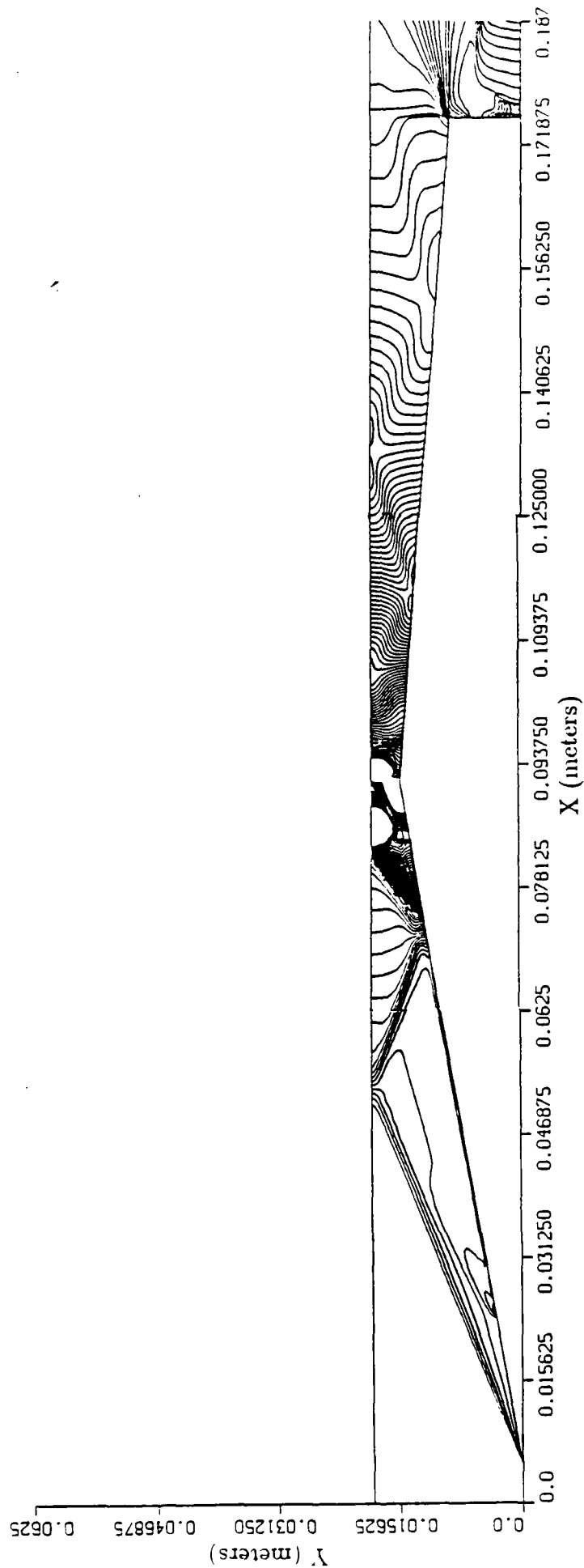**Figure 7.** Computed pressure contours for non-reacting turbulent flow, 38mm Config. 2, $M_\infty = 3.022, U_\infty = 1102\text{m/s}, P_\infty = 25\text{atm}, (.2 \leq P/P_\infty \leq 12, \triangle P = .1)$.
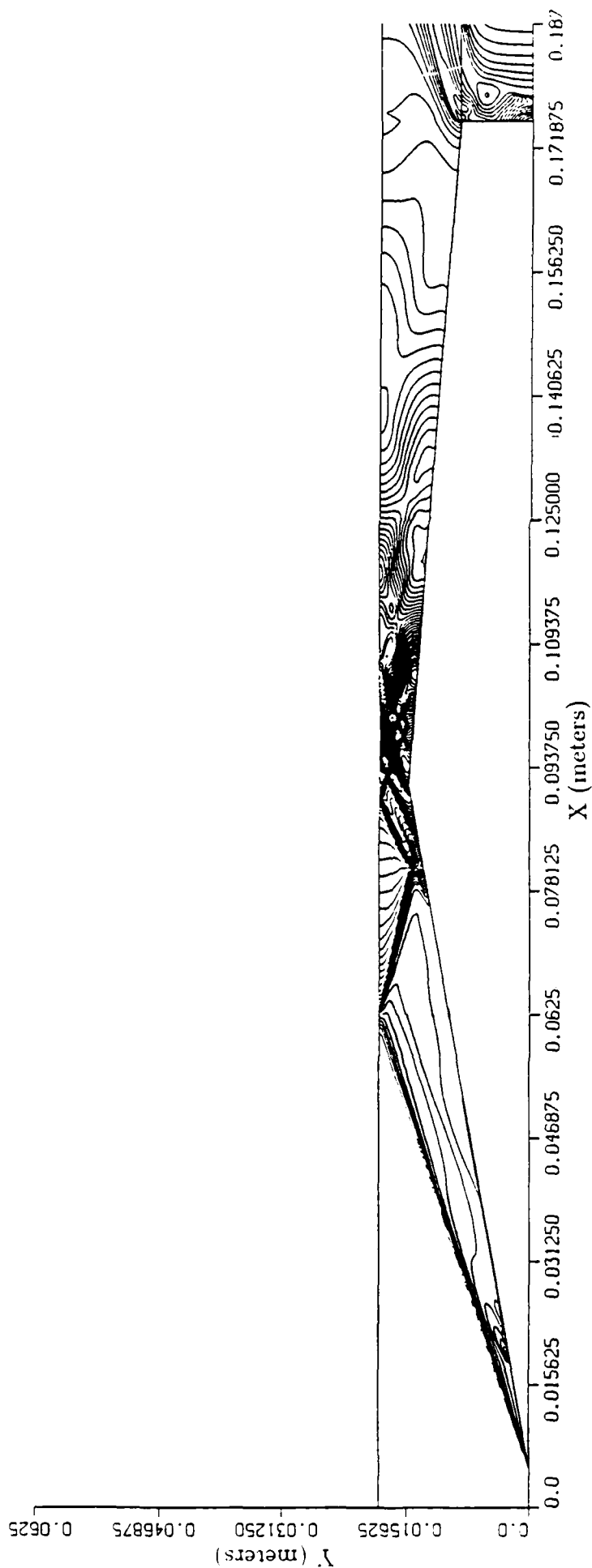
Figure 8. *Computed pressure contours for non-reacting turbulent flow, 38mm Config. 2,* $M_\infty = 3.95$, $U_\infty = 1430$m/s, $P_\infty = 20$atm, $(.2 \leq P/P_\infty \leq 12, \Delta P = .1)$.

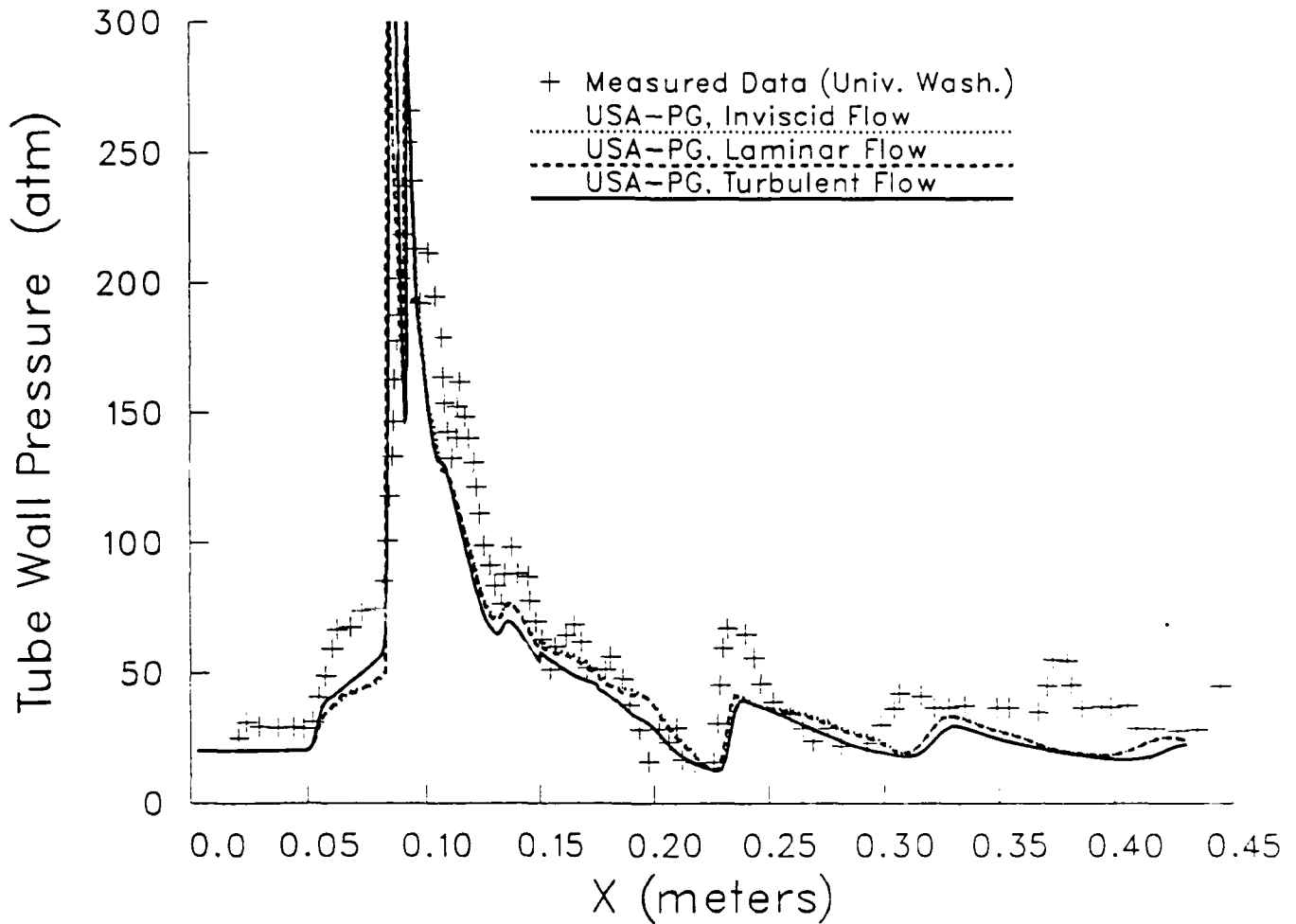**Figure 9.** Computed and measured tube wall pressures for non-reacting flow. 38mm Config. 2, $M_\infty = 3.022, U_\infty = 1102\text{m/s}, P_\infty = 25\text{atm}$.
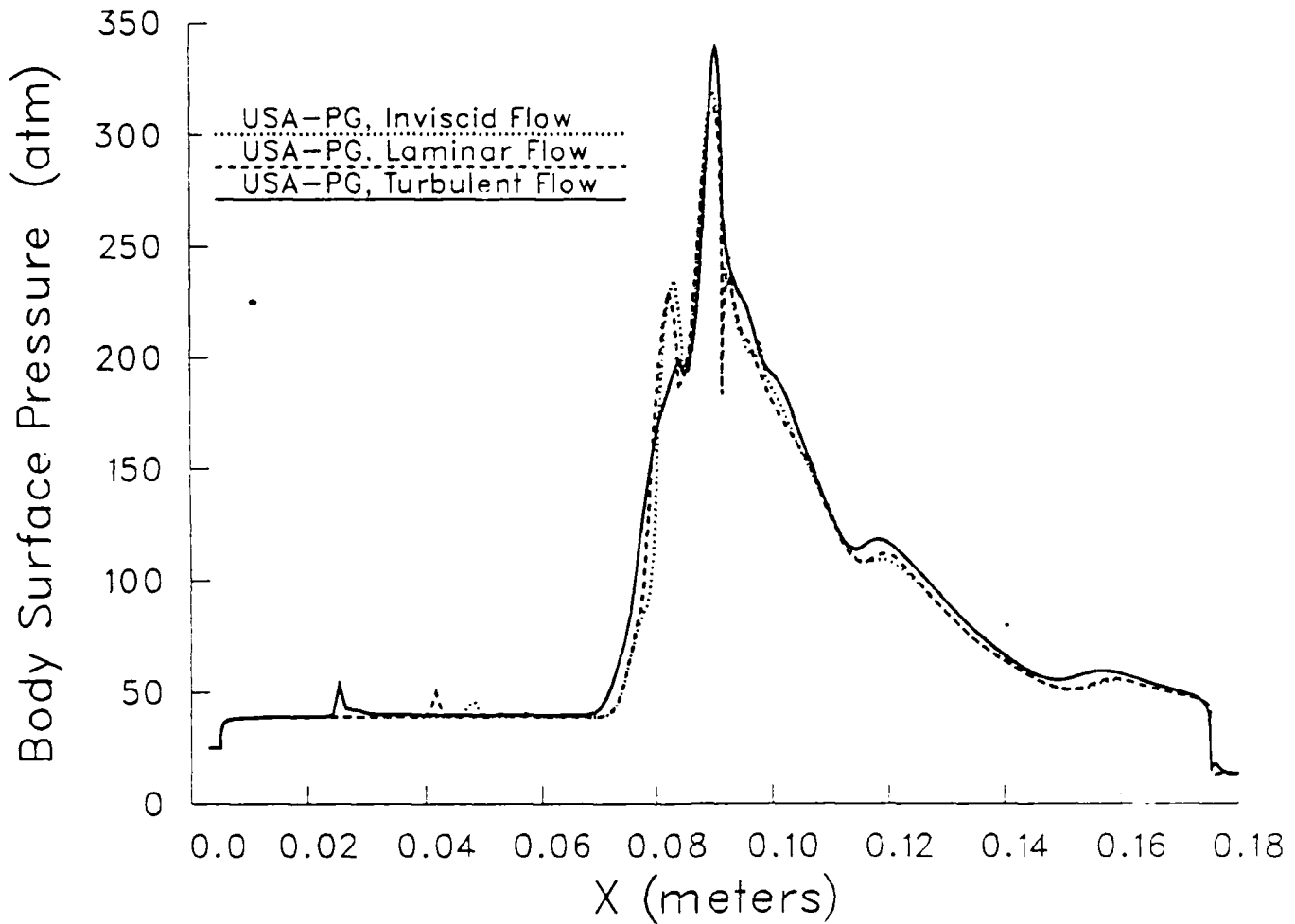
Figure 10. Computed body wall pressures for non-reacting flow, 38mm Config. 2. $M_\infty = 3.022, U_\infty = 1102\text{m/s}, P_\infty = 25\text{atm}$.

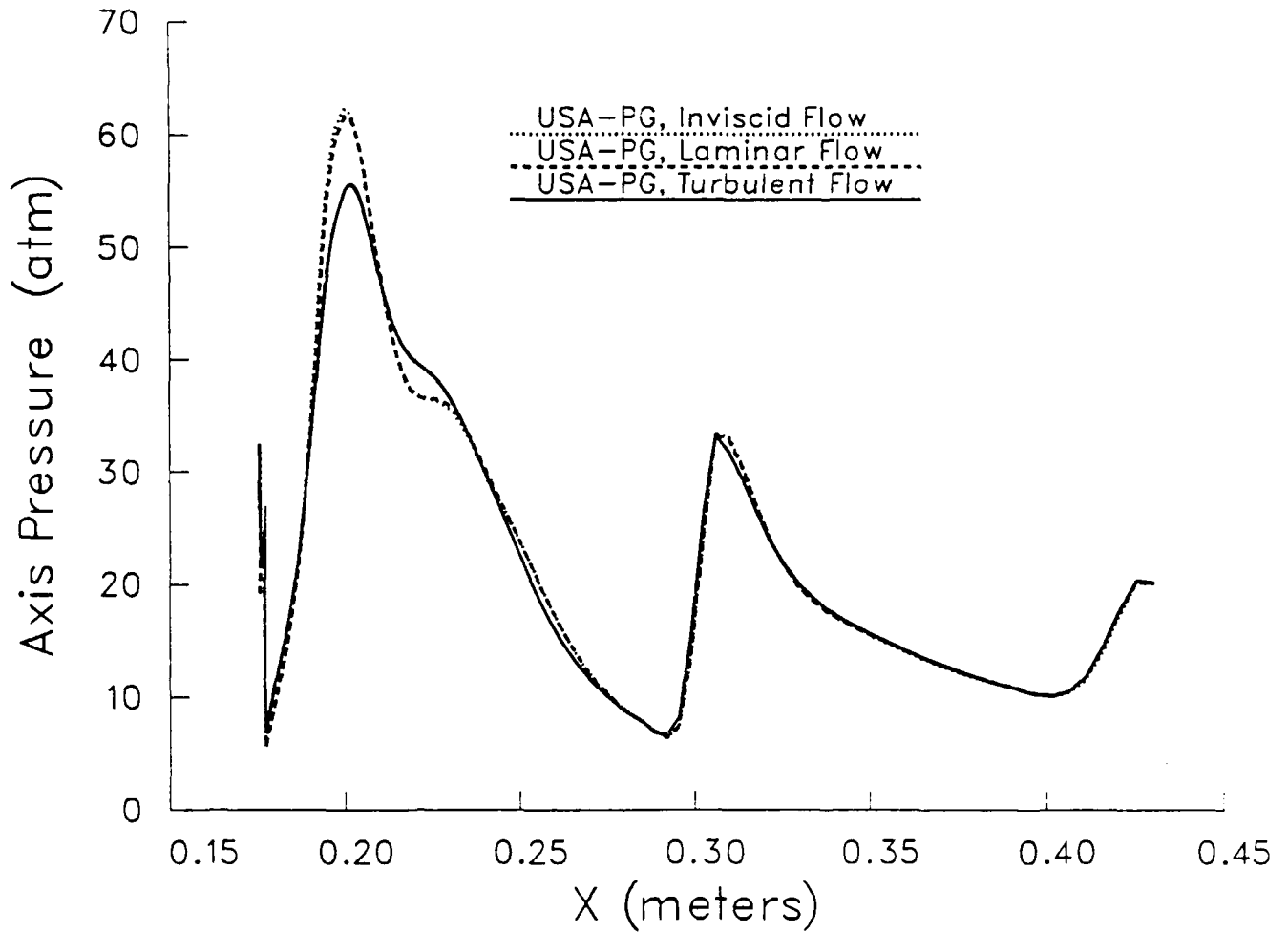Non−Reacting, 38mm, Config. #2
U = 1102 m/s, Mach = 3.022, P = 25 atm

Figure 11. Computed tube axis pressures for non-reacting flow, 38mm Config. 2, $M_\infty = 3.022, U_\infty = 1102 \text{m/s}, P_\infty = 25 \text{atm}$.

Figure 12. Computed tube wall pressures for non-reacting turbulent flow, 38mm Config. 1 and Config. 2, $M_\infty = 3.022, U_\infty = 1102\text{m/s}, P_\infty = 25\text{atm}$.

Figure 13. Computed tube wall pressures for non-reacting turbulent flow, 38mm Config. 2, $M_\infty = 3.022$ and $M_\infty = 3.95$.

31
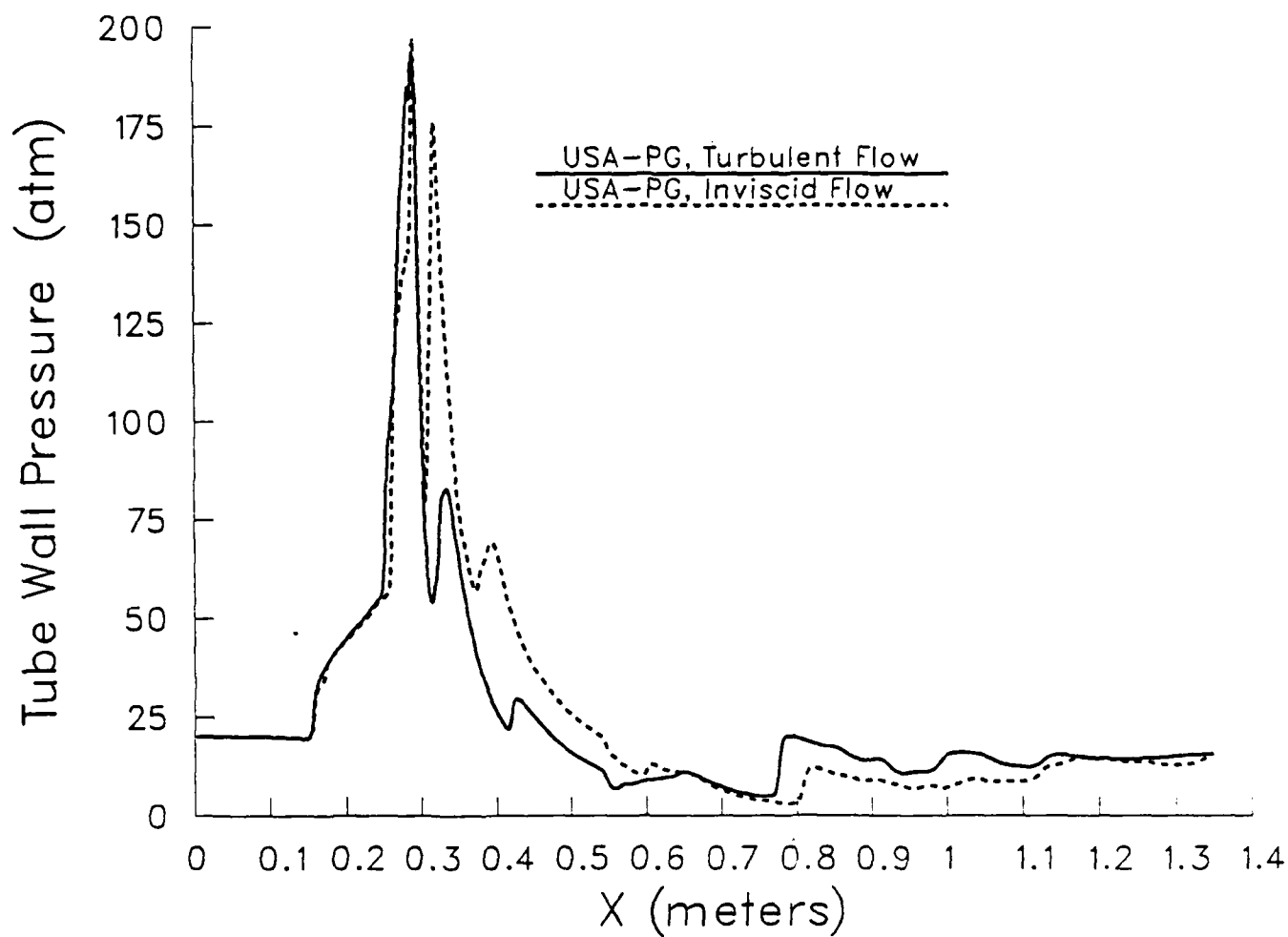
Figure 14. Computed tube wall pressures for non-reacting flow, 120mm Config. 2, $M_\infty = 3.022, U_\infty = 1102\mathrm{m/s}, P_\infty = 25\mathrm{atm}$.

Non—Reacting Flow, 120mm, Config. #1, #2
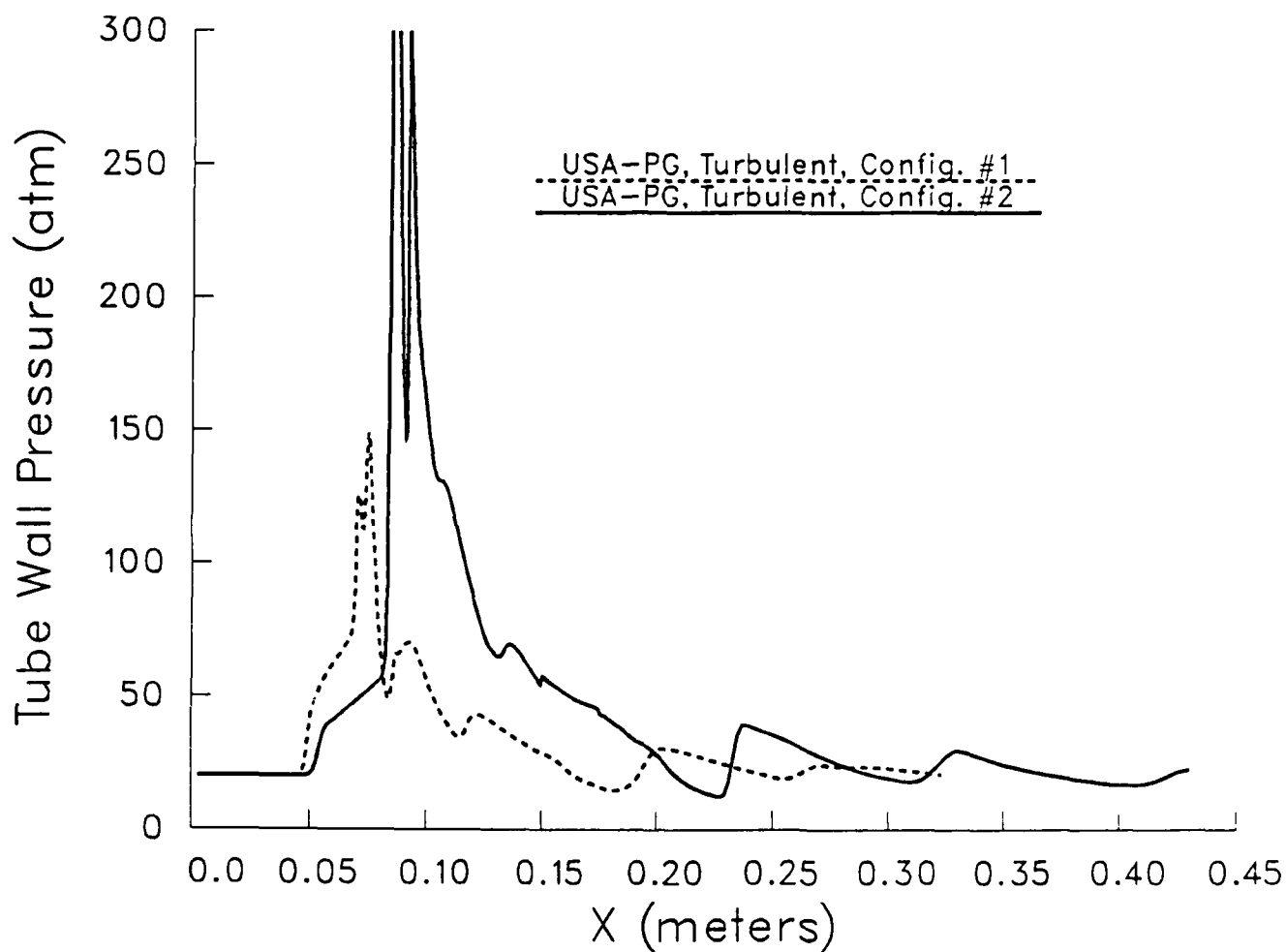U = 1102 m/s, Mach = 3.022, P = 25 atm
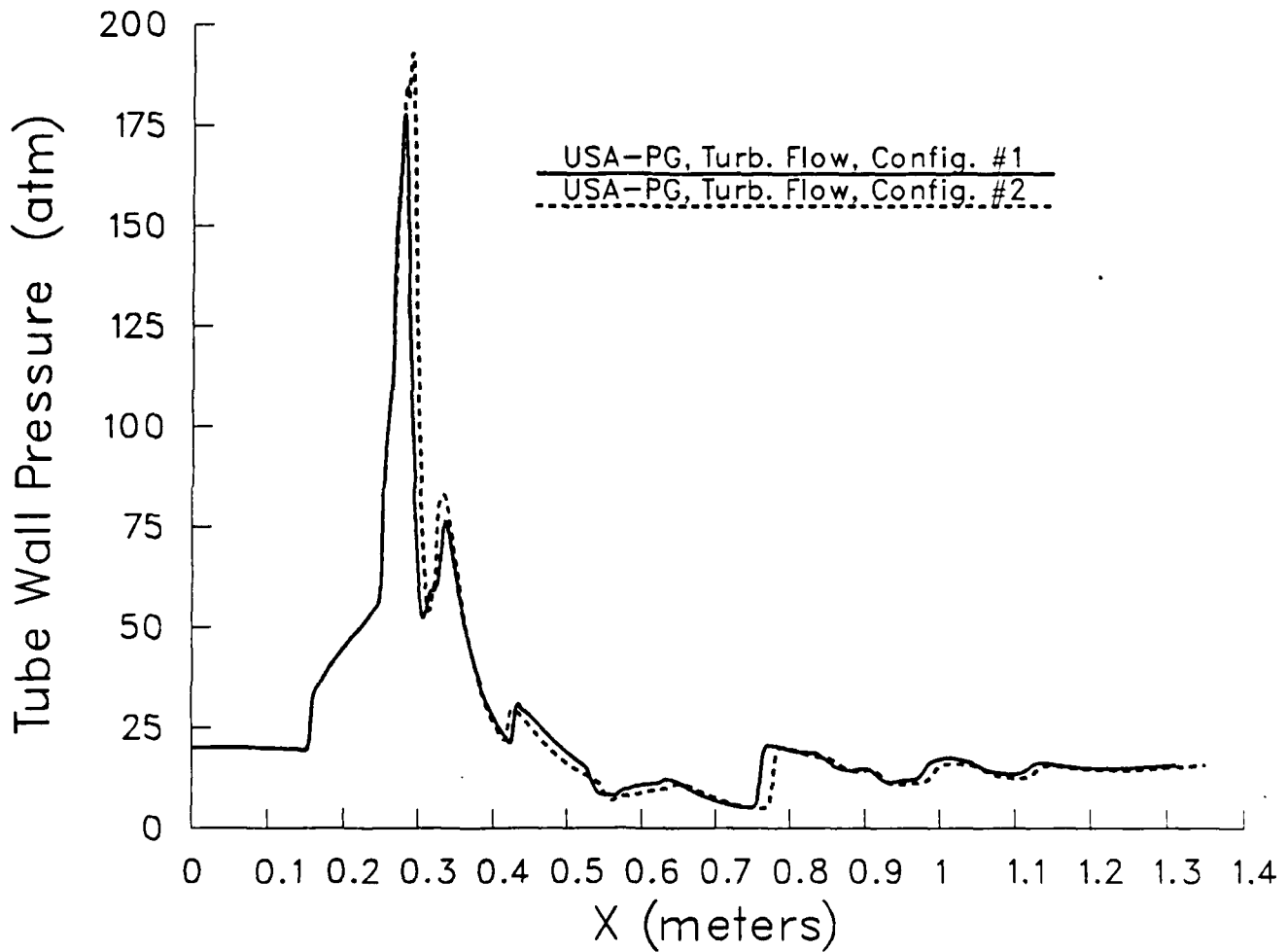
Figure 15. Computed tube wall pressures for non-reacting turbulent flow, 120mm Config. 1 and Config. 2, $M_\infty = 3.022, U_\infty = 1102 \text{m/s}, P_\infty = 25 \text{atm}$.

33
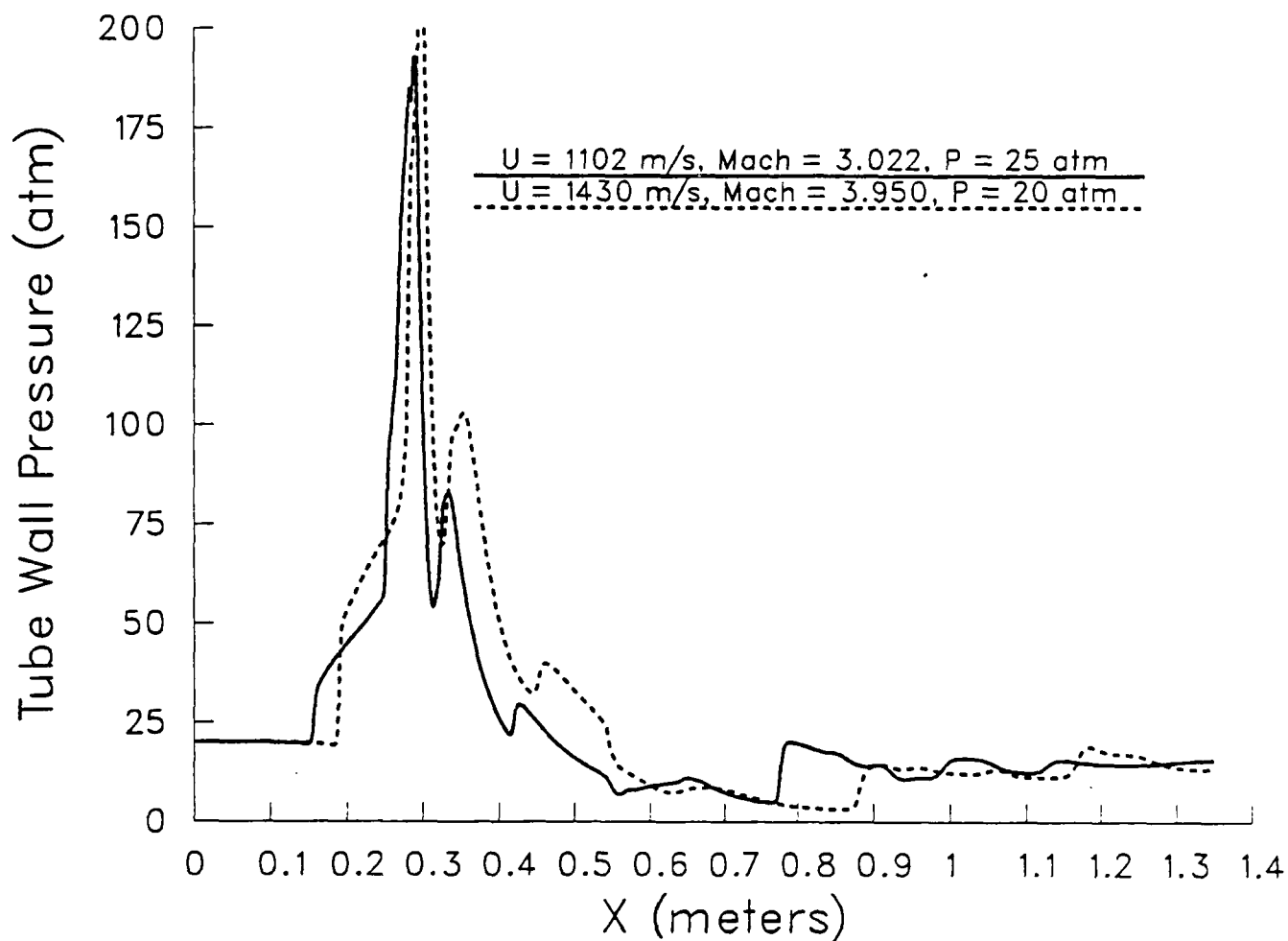
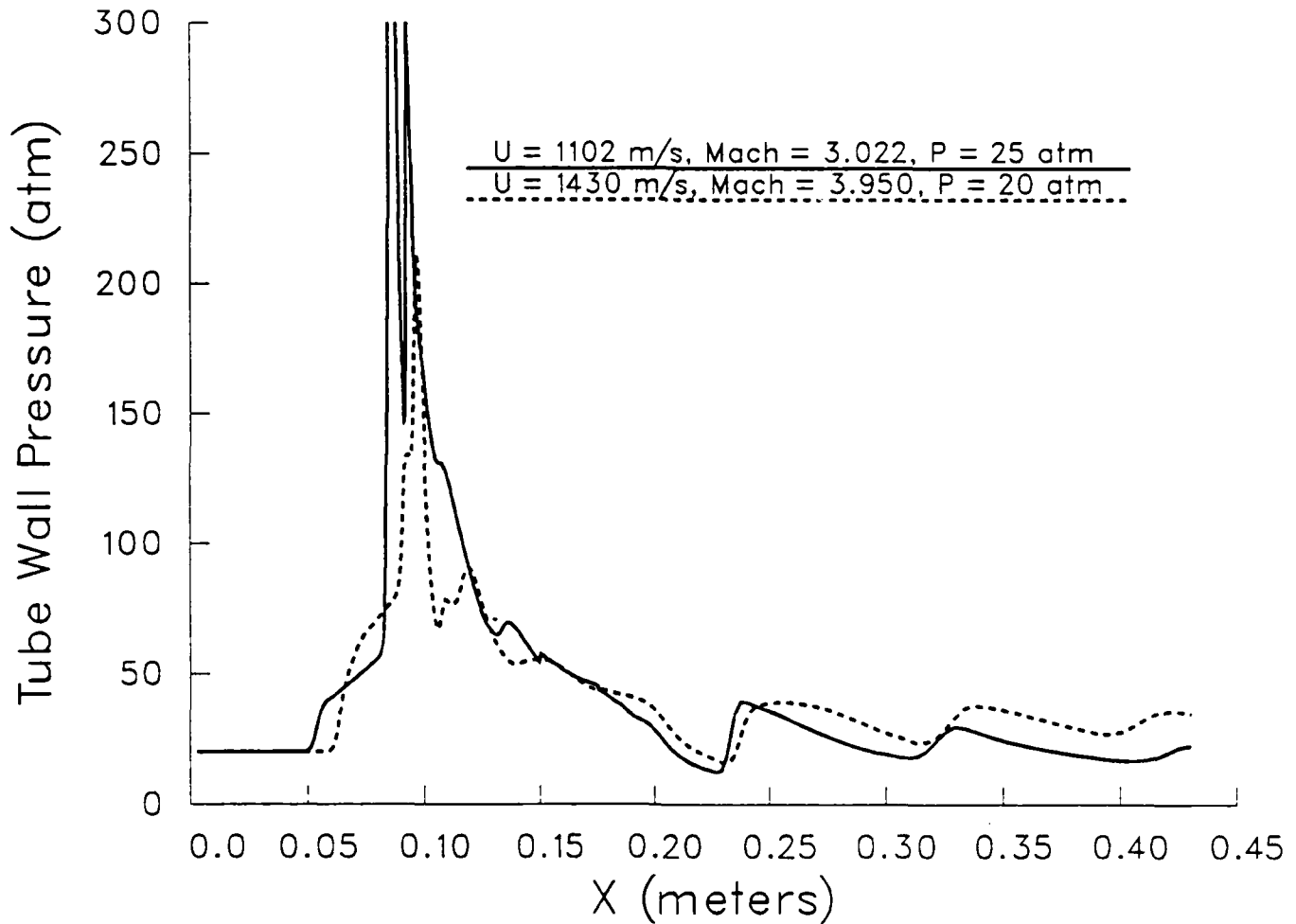**Figure 16.** Computed tube wall pressures for non-reacting turbulent flow, 120mm Config. 2, $M_\infty = 3.022$ and $M_\infty = 3.95$.
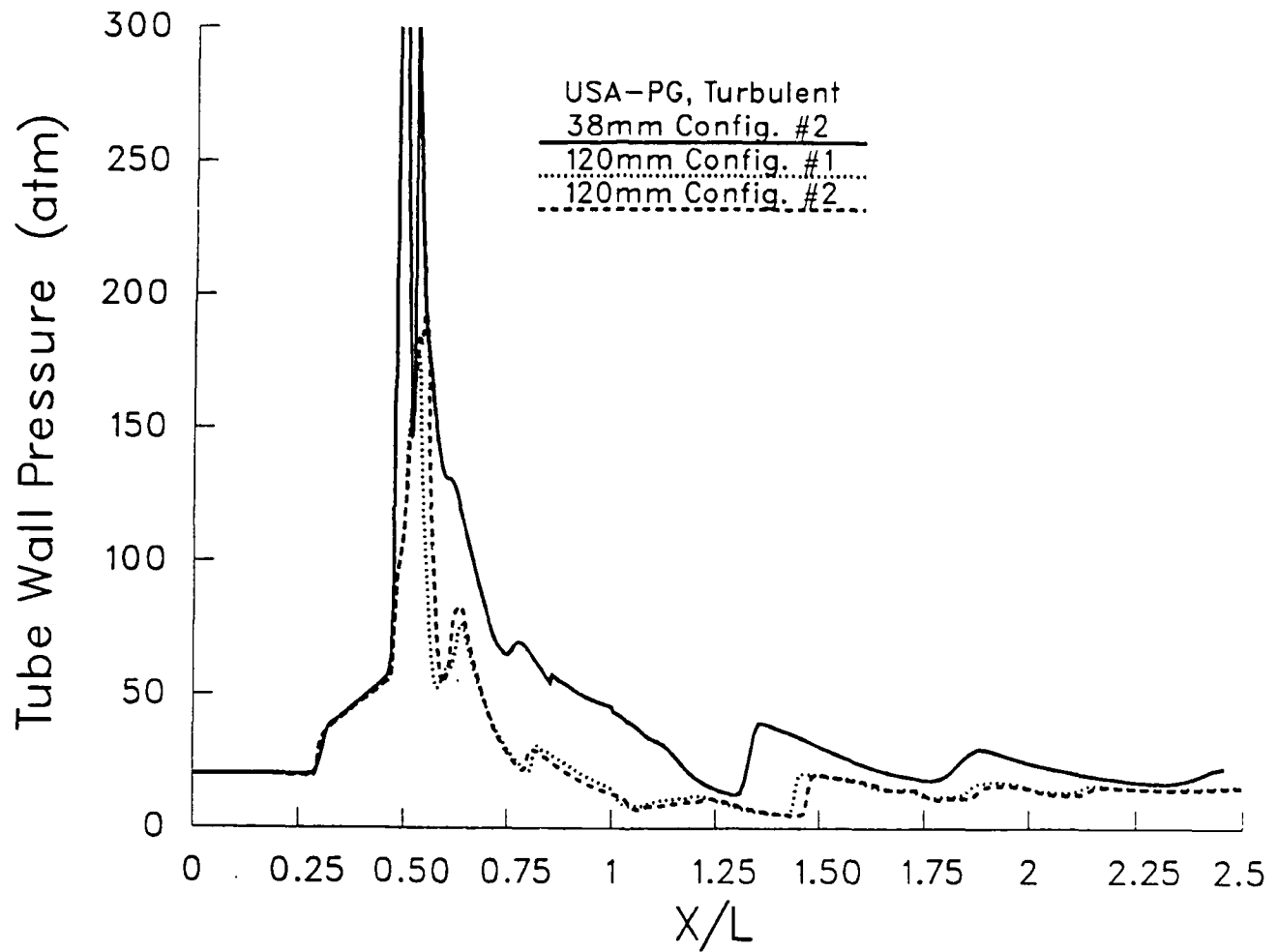
Figure 17. Computed tube wall pressures for non-reacting turbulent flow, 38mm Config. 2, 120mm Config. 1 and Config. 2, $M_\infty = 3.022, U_\infty = 1102$m/s, $P_\infty = 25$atm.

Non-Reacting Case
U = 1430 m/s, Mach = 3.95, P = 20 atm
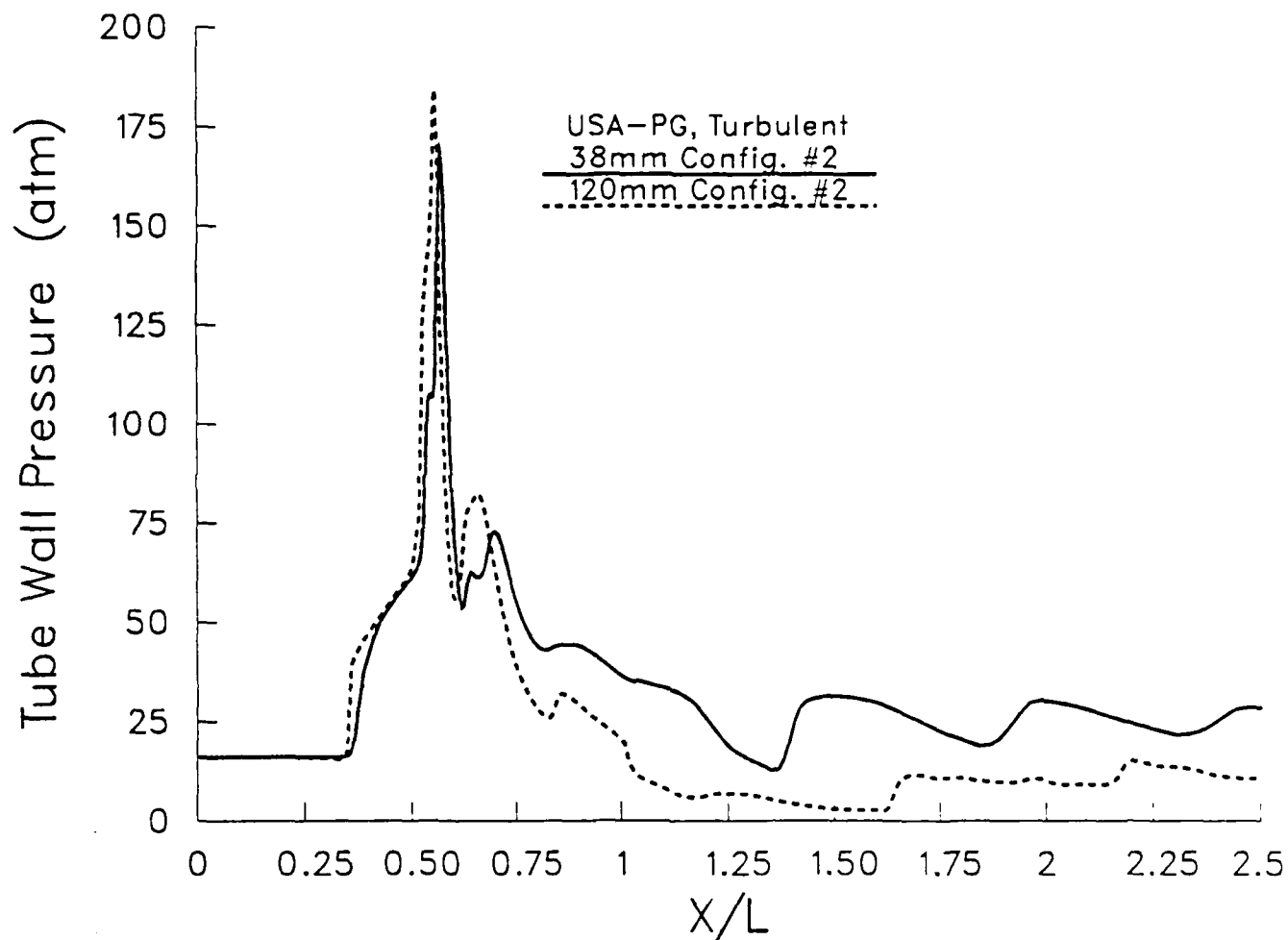
Figure 18. Computed tube wall pressures for non-reacting turbulent flow, 38mm Config. 2 and 120mm Config. 2, $M_\infty = 3.95, U_\infty = 1430\text{m/s}, P_\infty = 20\text{atm}$.

Figure 19. Computed and measured tube wall pressures for reacting flow, 38mm Config. 2, $M_\infty = 3.95$, $U_\infty = 1430\text{m/s}$, $P_\infty = 20\text{atm}$.

38mm Config. #2, 120mm Config. #2
U = 1430 m/s, Mach = 3.95, P = 20 atm
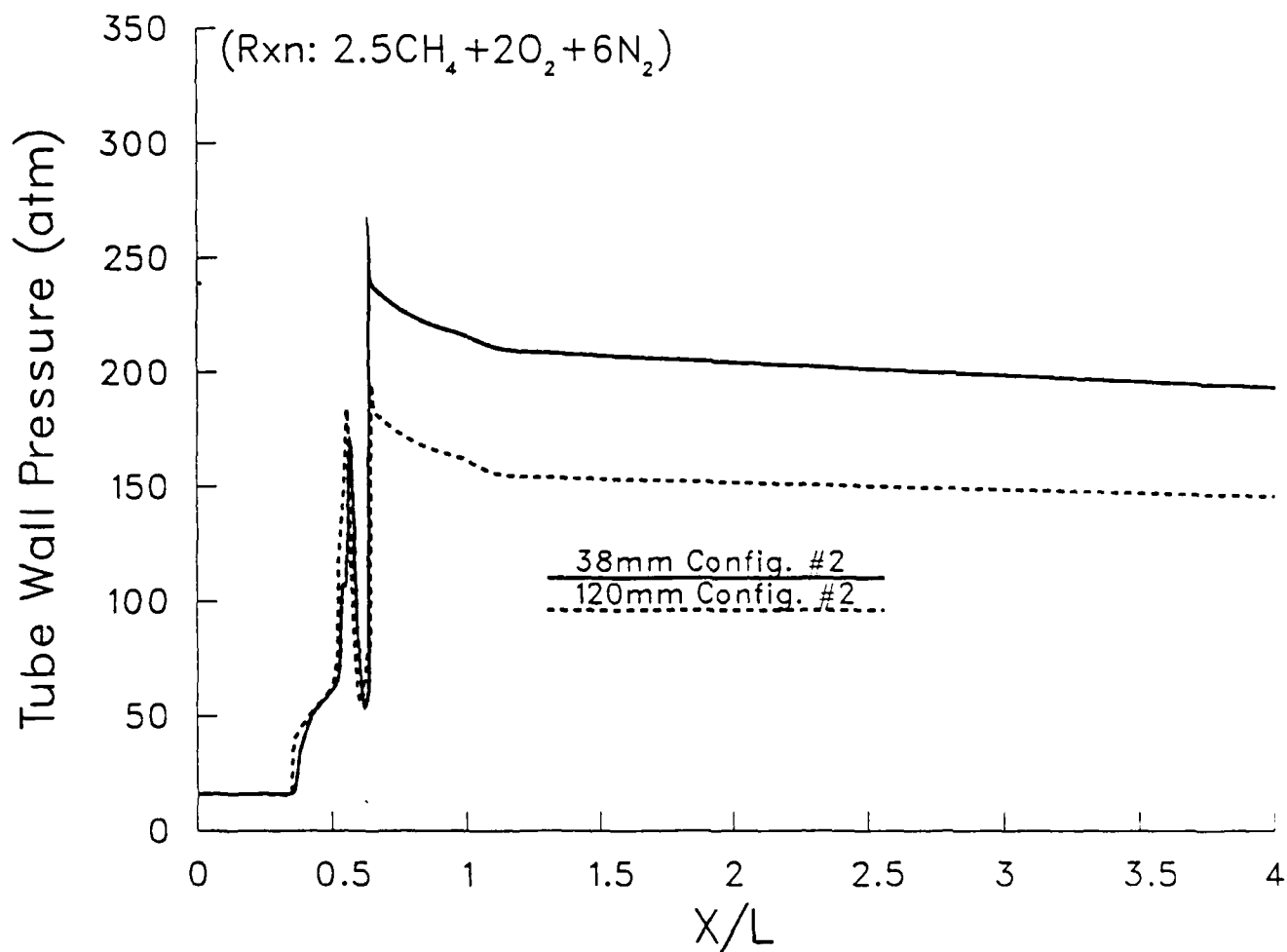
Figure 20. Computed tube wall pressures for reacting flow, 38mm Config. 2. 120mm Config. 2, $M_\infty = 3.95, U_\infty = 1430\text{m/s}, P_\infty = 20\text{atm}$.
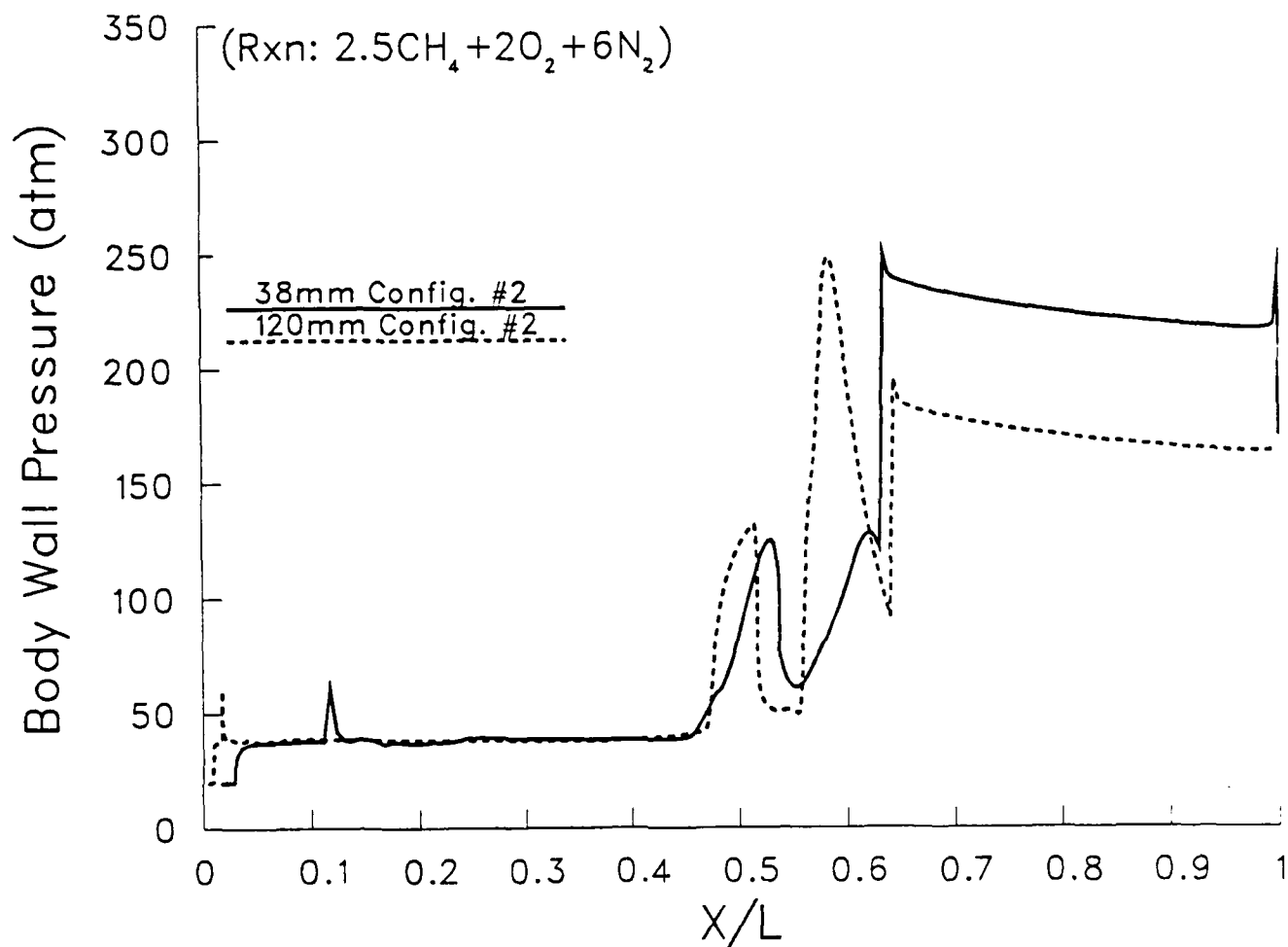
Figure 21. Computed body wall pressures for reacting flow, 38mm Config. 2. 120mm Config. 2, $M_\infty = 3.95, U_\infty = 1430\text{m/s}, P_\infty = 20\text{atm}.$
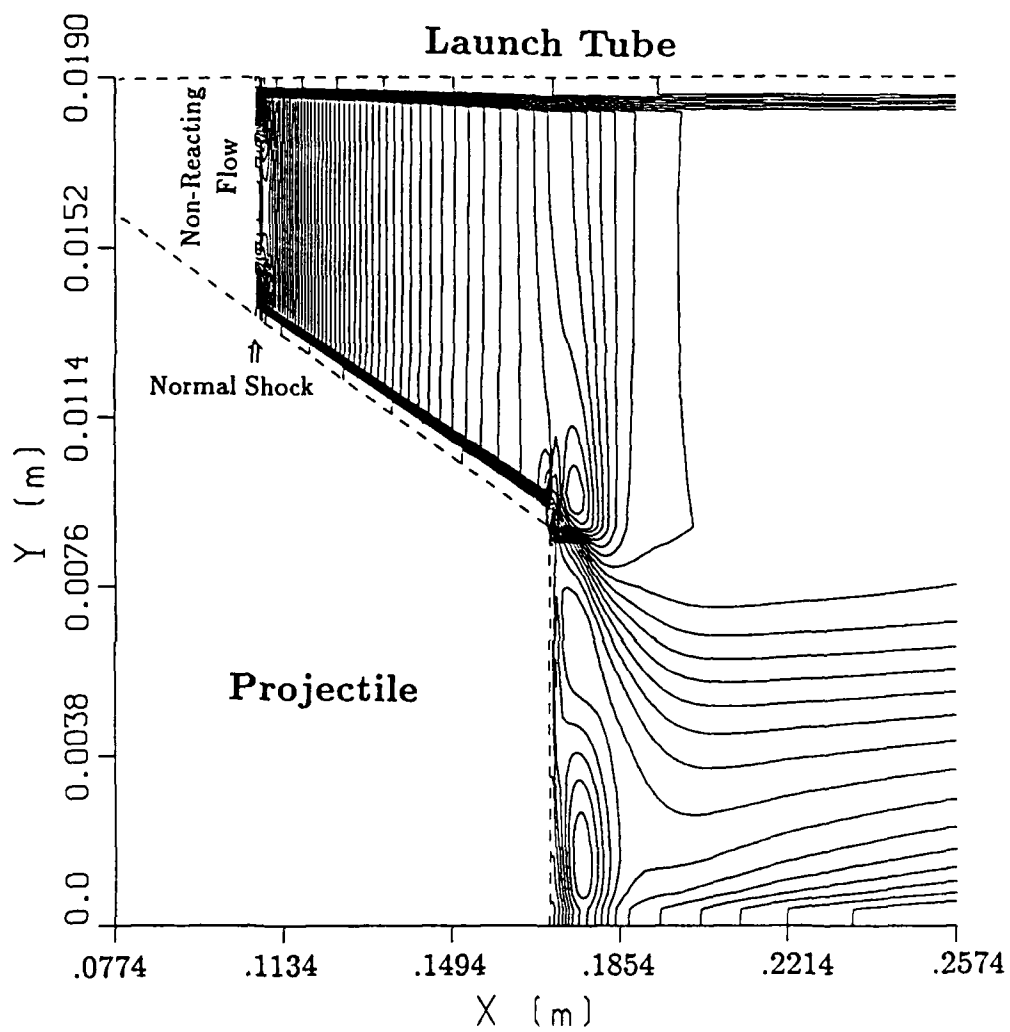
Figure 22. Computed reaction rate contours for reacting flow, 38mm Config. 2, $M_\infty = 3.95, U_\infty = 1430\text{m/s}, P_\infty = 20\text{atm}.$

Figure 23. Computed product mass fraction contours for reacting flow, 38mm Config. 2, $M_\infty = 3.95, U_\infty = 1430\text{m/s}, P_\infty = 20\text{atm}$.

INTENTIONALLY LEFT BLANK.

References

1. Bruckner, A.P., Bogdanoff, D.W., Knowlen, C., and Hertzberg, A., "Investigation of Gasdynamic Phenomena Associated with the Ram Accelerator Concept," AIAA-87-1327, Proceedings of the AIAA 19th Fluid Dynamics, Plasma Dynamics and Lasers Conference, June 8-10, 1987, Honolulu, Hawaii.
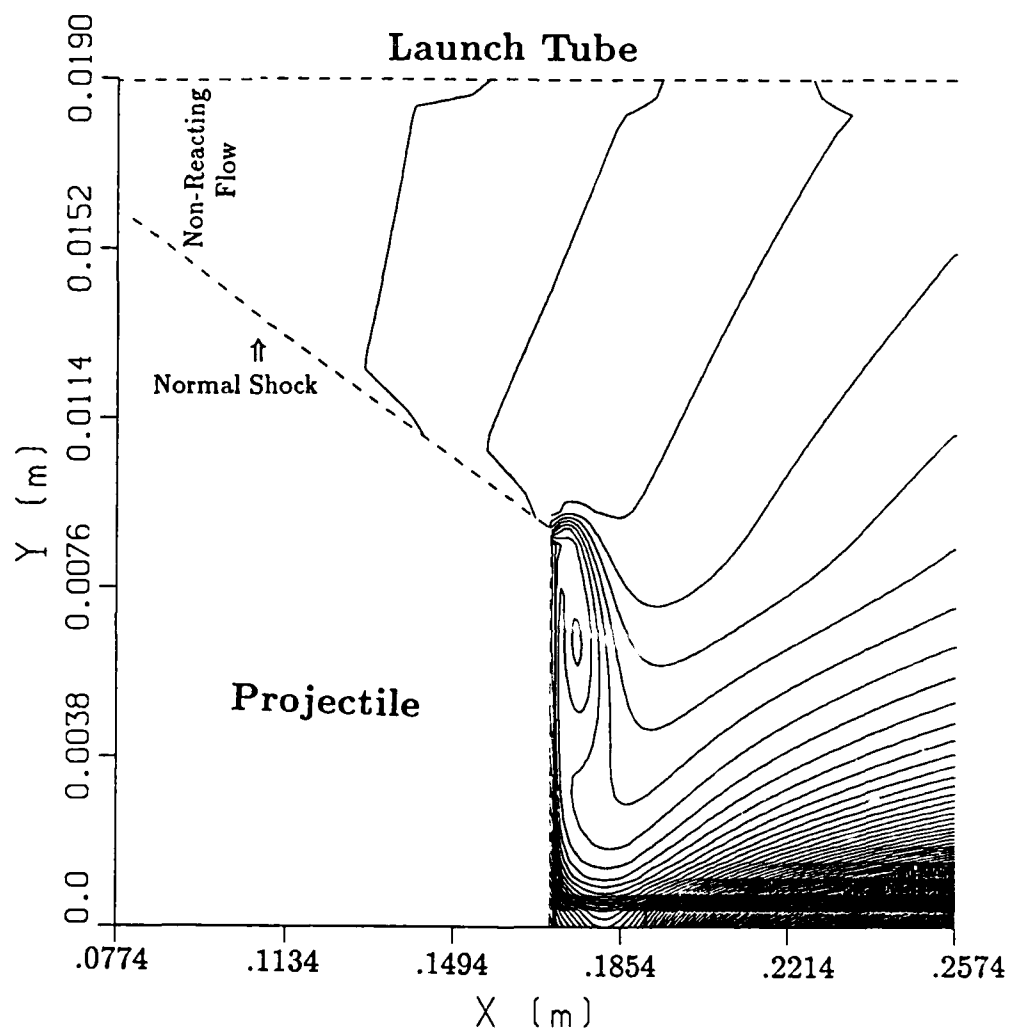
2. Hertzberg, A., Bruckner, A.P., and Bogdanoff, D.W., "Ram Accelerator: A New Chemical Method for Accelerating Projectiles to Ultrahigh Velocities," AIAA Journal, Vol. 26, No. 2, Feb. 1988, pp. 195-203.

3. Bruckner, A.P., Knowlen, C., Scott, K.A., and Hertzberg, A., "High Velocity Modes of the Thermally Choked Ram Accelerator," AIAA-88-2925, Proceedings for the AIAA 24th Joint Propulsion Conference July 11-13, 1988, Boston, MA.

4. Burnham, E.A., Kull, A.E., Knowlen, C., Bruckner, A.P., and Hertzberg, A., "Operation of the Ram Accelerator in the Transdetonative Velocity Regime," AIAA-90-1985, Proceedings for the AIAA 26th Joint Propulsion Conference, July 16-18, 1990, Orlando, FL.

5. Bruckner, Hertzberg, A., and Knowlen, C., "Review of Ram Accelerator Propulsion Modes," Proceedings of the 27th JANNAF Combustion Subcommittee Meeting, November 5-9, 1990, Warren AFB, Cheyenne, WY.

6. Kruczynski, D.L., "Large Caliber Applications of Ram Accelerator Technology," Proceedings of the 27th JANNAF Combustion Subcommittee Meeting, November 5-9, 1990, Warren AFB, Cheyenne, WY.

7. Nusca, M.J., "Numerical Simulation of Reacting Flow in a Thermally Choked Ram Accelerator," Proceedings of the 27th JANNAF Combustion Subcommittee Meeting, November 5-9, 1990, Warren AFB, Cheyenne, WY.

8. Chakravarthy, S.R., Szema, K.Y., Goldberg, U.C., Gorski, J.J., and Osher, S., "Application of a New Class of High Accuracy TVD Schemes to the Navier-Stokes Equations," AIAA-85-0165, Proceedings of the AIAA 23rd Aerospace Sciences Meeting, Jan. 14-17, 1985, Reno, NV.

9. Chakravarthy, S.R., Szema, K.Y., and Haney, J.W., "Unified Nose-to-Tail Computational Method for Hypersonic Vehicle Applications," AIAA-89-2564, Proceedings of the AIAA 6th Applied Aerodynamics Conference, June 6-8, 1989, Williamsburg, VA.

10. Nusca, M.J., Chakravarthy, S.R. Goldberg, U.C., "Computational Fluid Dynamics Capability for the Solid-Fuel Ramjet Projectile," AIAA Journal of Propulsion and Power, Vol. 6, No. 3, May-June 1990, pp. 256-262 (see also AIAA-87-2411 and U.S. Army Ballistic Research Laboratory report BRL-TR-2958, Dec. 1988).

11. Nusca, M.J., "Steady Flow Combustion Model for Solid-Fuel Ramjet Projectiles," AIAA Journal of Propulsion and Power, Vol. 6, No. 3, May-June 1990, pp. 348-352 (see also AIAA-89-2797 and U.S. Army Ballistic Research Laboratory report BRL-TR-2987, April 1989).

12. Bogdanoff, D.W., and Brackett, D.C., "A Computational Fluid Dynamics Code for the Investigation of Ramjet-In-Tube Concepts," AIAA-87-1978, Proceedings of the AIAA 23rd Joint Propulsion Conference, June 29-July 2, 1987, San Diego, CA.

13. Yungster, S., Eberhardt, S., and Bruckner, A.P., "Numerical Simulation of Shock-Induced Combustion Generated by High-Speed Projectiles in Detonable Gas Mixtures," AIAA-89-0673, Proceedings of the AIAA 27th Aerospace Sciences Meeting, Jan. 9-12, 1989, Reno, NV.

14. Yungster, S., and Bruckner, A.P., "A Numerical Study of the Ram Accelerator Concept in the Superdetonative Velocity Range," AIAA-89-2677, Proceedings of the AIAA 25th Joint Propulsion Conference, July 10-12, 1989, Monterey, CA.

15. Chuck, C., and Eberhardt, S., "Numerical Simulation of Hypersonic Oblique Shock-Wave/Laminar Boundary-Layer Interaction with Shock Induced Combustion," AIAA-90-0149, Proceedings of the AIAA 28th Aerospace Sciences Meeting, Jan. 8-11, 1990, Reno, NV.

16. Ota, D.K., Chakravarthy S.R., and Darling, J.C., "An Equilibrium Air Navier-Stokes Code for Hypersonic Flows," AIAA-88-0419, Proceedings of the 26th AIAA Aerospace Sciences Meeting, Reno, NV, January 11-14, 1988.

17. Palaniswamy, S., and Chakravarthy, S.R., "Finite Rate Chemistry for USA Series Codes: Formulation and Applications," AIAA-89-0200, Proceedings of the 27th AIAA Aerospace Sciences Meeting, Reno, NV, January 9-12, 1989.

18. Baldwin, B.S. and Lomax, H., "Thin Layer Approximation and Algebraic Model for Separated Turbulent Flows," AIAA-78-257, Proceedings of the 16th AIAA Aerospace Sciences Meeting, Huntsville, AL, January 16-18, 1978.

19. Goldberg U.C., "Separated Flow Treatment with a New Turbulence Model," AIAA Journal, Vol. 24, No. 10, October 1986, pp. 1711-1713.

20. Mazor G., Ben-Dor G., and Igra O., "A Simple and Accurate Expression for the Viscosity of Nonpolar Diatomic Gases up to 10,000 K," AIAA Journal, Vol. 23, No. 4, April 1985, pp. 636-638.

21. Goldberg, U.C., "Separated Flows Calculations With A New Turbulence Model," presented at the IACM First World Congress on Computational Mechanics, Austin, TX, Sept. 1986.

22. Goldberg, U.C., "Prediction of Separated Flows With A New Turbulence Model," AIAA Journal, Vol. 26, No. 4, April 1988, pp. 405-408.

23. Schlichting, H., Boundary Layer Theory, 7th ed., translated by J. Kestin, McGraw-Hill, New York, 1979.

24. Bradshaw, P., Cebeci, T., and Whitelaw, J.H., Engineering Calculation Methods for Turbulent Flows, Academic Press, New York, 1981.

25. Ames Research Staff, "Equations, Tables, and Charts for Compressible Flow," NACA Report 1135, 1958.

26. Kim, Y.M., and Chung, T.J., "Finite-Element Analysis of Turbulent Diffusion Flames," AIAA Journal, Vol. 27, No. 3, March 1989, pp. 330-339.

27. Rogers, R.C., and Chinitz, W., "Using a Global Hydrogen-Air Combustion Model in Turbulent Reacting Flow Calculations," AIAA Journal, Vol. 21, No. 4, April 1983, pp. 586-592.

28. Khalil, E.E., Spalding, D.B., and Whitelaw, J.H., "The Calculation of Local Flow Properties in Two-Dimensional Furnaces," International Journal of Heat and Mass Transfer, 1975, Vol. 18, pp. 775-791.

29. Kuo, K.K., Principles of Combustion, John Wiley and Sons, Inc., New York, 1986.

30. Williams, F.A., Combustion Theory, Addison-Wesley Publishing Company, Inc., 1965.

31. Westbrook, C.K., and Dryer, F.L., "Chemical Kinetic Modeling of Hydrocarbon Combustion," Progress in Energy Combustion Science, Vol. 10, pp. 1-57.

32. Kivity, Y., Grimberg, M., and Halevy, D., "Performance of the Ram Accelerator in the Oblique Detonation Mode," Proceedings of the 41st Meeting of the Aeroballistic Range Association, San Diego, CA, Oct. 22-25, 1990.

33. Carnahan, B., Luther, H.A., and Wilkes, J.O., Applied Numerical Methods, John Wiley and Sons, New York, 1969.

INTENTIONALLY LEFT BLANK.

List of Symbols

A	cross sectional area of launch tube
c_p	specific heat capacity, constant p
c_v	specific heat capacity, constant volume
C	specific reaction rate constant
e	specific total internal energy
E_a	activation energy
F, G, H	flux vectors (Eq. 1)
h	molar specific enthalpy
$\tilde{h}$	total enthalpy
J	flow rate or flux
k	turbulence kinetic energy
L	total body length
m	species mass fraction
M	Mach number
$\mathcal{M}$	molecular weight .
n	stoichiometric coefficient
N	number of species
p	static pressure
Pr	Prandtl Number
$\dot{q}$	heat transfer rate
r	radial direction
R	reaction rate per unit volume
$\Re$	specific gas constant, $(\gamma - 1)c_p/\gamma$
$\bar{\Re}$	universal gas constant, $\Re_{\cdot j}\,\mathcal{M}_j$
Re	Reynolds Number
Sc	Schmidt Number
t	time
T	static temperature
$\mathcal{T}$	thrust
u	axial velocity (USA-PG code); radial velocity (RAMCOMB code)
U	mean streamwise velocity
v	radial velocity (USA-PG code); azimuthal velocity (RAMCOMB code)
V	magnitude of the local velocity vector
$\vec{V}$	$u\hat{r} + v\hat{\theta} + w\hat{z}$
w	velocity component in the axial direction
W	dependent variable vector (Eq. 1)
x, y	cartesian coordinates
z	axial direction
ΔH_f^o	heat of formation
ΔH_r	heat of reaction

Greek Symbols

γ	ratio of specific heats, c_p/c_v

Γ	diffusion coefficient
δ	stoichiometric air/fuel mass ratio
ϵ	turbulence dissipation rate
η	transformed coordinate
θ	azimuthal direction
μ	molecular viscosity
ξ	transformed coordinate
ρ	density
σ_h	$\mu_{\text{eff}}/\Gamma_h$
σ_j	$\mu_{\text{eff}}/\Gamma_j$
σ_k	$\mu_{\text{eff}}/\Gamma_k$
σ_{xx}, σ_{rr}	normal stress tensors
τ	transformed time
τ_{xr}	shear stress tensor
$\vec{\tau}$	shear stress vector
ϕ	general flow variable
ψ	stream function
ω	vorticity

Superscripts

$\hat{}$	unit vector
$\tilde{}$	total or stagnation
$\dot{}$	rate

Subscripts

eff	effective
f	adiabatic flame quantity
h	enthalpy
i	initial or base-state quantity
j	j-th mixture component or species
k	turbulence kinetic energy
p	constant pressure
r	radial component or radial direction
t	turbulence quantity
v	constant volume
x	x-direction
z	axial component
ϵ	turbulence dissipation rate
η	η-direction transform coefficient
θ	azimuthal component
ξ	ξ-direction transform coefficient
∞	freestream quantity

2	Administrator Defense Technical Info Center ATTN: DTIC-DDA Cameron Station Alexandria, VA 22304-6145
1	HQDA (SARD-TR) WASH DC 20310-0001
1	Commander U.S. Army Materiel Command ATTN: AMCDRA-ST 5001 Eisenhower Avenue Alexandria, VA 22333-0001
1	Commander U.S. Army Laboratory Command ATTN: AMSLC-DL 2800 Powder Mill Road Adelphi, MD 20783-1145
2	Commander U.S. Army Armament Research, Development, and Engineering Center ATTN: SMCAR-IMI-I Picatinny Arsenal, NJ 07806-5000
2	Commander U.S. Army Armament Research, Development, and Engineering Center ATTN: SMCAR-TDC Picatinny Arsenal, NJ 07806-5000
1	Director Benet Weapons Laboratory U.S. Army Armament Research, Development, and Engineering Center ATTN: SMCAR-CCB-TL Watervliet, NY 12189-4050
1	Commander U.S. Army Armament, Munitions and Chemical Command ATTN: SMCAR-ESP-L Rock Island, IL 61299-5000
1	Director U.S. Army Aviation Research and Technology Activity ATTN: SAVRT-R (Library) M/S 219-3 Ames Research Center Moffett Field, CA 94035-1000

1	Commander U.S. Army Missile Command ATTN: AMSMI-RD-CS-R (DOC) Redstone Arsenal, AL 35898-5010
1	Commander U.S. Army Tank-Automotive Command ATTN: ASQNC-TAC-DIT (Technical Information Center) Warren, MI 48397-5000
1	Director U.S. Army TRADOC Analysis Command ATTN: ATRC-WSR White Sands Missile Range, NM 88002-5502
(Class. only)1	Commandant U.S. Army Infantry School ATTN: ATSH-CD (Security Mgr.) Fort Benning, GA 31905-5660
(Unclass. only)1	Commandant U.S. Army Infantry School ATTN: ATSH-CD-CSO-OR Fort Benning, GA 31905-5660
1	Air Force Armament Laboratory ATTN: AFATL/DLODL Eglin AFB, FL 32542-5000

Aberdeen Proving Ground

2	Dir, USAMSAA ATTN: AMXSY-D AMXSY-MP, H. Cohen
1	Cdr, USATECOM ATTN: AMSTE-TD

3	Cdr, CRDEC, AMCCOM
	ATTN: SMCCR-RSP-A
	        SMCCR-MU
	        SMCCR-MSI

1	Dir, VLAMO ATTN: AMSLC-VL-D
10	Dir, BRL ATTN: SLCBR-DD-T

No. of Copies	Organization	No. of Copies	Organization
1	OSD/SDIO/IST ATTN: Dr. L. Caveny The Pentagon Washington, DC 20301-7100	1	Director NASA Langley Research Center ATTN: Technical Library Langley Station Hampton, VA 23665
1	Commander US Army, ARDEC ATTN: SMCAR-FSP-A, R. Kline Picatinny Arsenal, NJ 07806-5000	2	Director NASA Langley Research Center ATTN: Mail Stop 408 W. Scallion R. Witcofski Langley Station
1	Commander US Army, ARDEC ATTN: SMCAR-AEE, D. Downs Picatinny Arsenal, NJ 07806-5000		Hampton, VA 23665
1	Commander Defense Advanced Research Projects Agency ATTN: MAJ R. Lundberg 1400 Wilson Blvd. Arlington, VA 22209	1	Director Sandia National Laboratories ATTN: W. Oberkampf Division 1636 Albuquerque, NM 87185
		1	Advanced Projects Research, Inc. ATTN: Dr. J. Humphrey, Suite A 5301 N. Commerce Avenue Moorpark, CA 93021
1	US Army Research Office Engineering Services Division ATTN: Dr. D.M. Mann P.O. Box 12211 Research Triangle Park, NC 27709-2211	2	Aerojet General Corporation ATTN: W. Wolterman S. Rush P.O. Box 296
1	US Army Space Technology and Research Office ATTN: COL D.S. Jackson 5321 Riggs Road Gaithersburg, MD 20882		Azusa, CA 91702
		1	Aerospace Corporation Aero-Engineering Subdivision ATTN: Walter F. Reddall El Segundo, CA 92045
1	AFOSR/NA ATTN: Dr. J. Tishkoff Bolling AFB, DC 20332-6448	1	Arrow Technology Associates, Inc. ATTN: R. Whyte P.O. Box 4218
1	Air Force Armament Laboratory ATTN: AFATL/FXA, G.L. Winchenbach Eglin AFB, FL 32542-5434		South Burlington, VT 05401-0042
		1	Calspan Corporation ATTN: W. Rae P.O. Box 400
1	Air Force Armament Laboratory ATTN: AFATL/FXP, C.J. Cottrell Eglin AFB, FL 32542-5434		Buffalo, NY 14225
1	Air Force Armament Laboratory ATTN: AFATL/SAH, CPT R. Drabczuk Eglin AFB, FL 32542-5434	1	EPR ATTN: Dr. J.D. Kuzan P.O. Box 2180 Houston, TX 77252-2180

2	Olin Ordnance ATTN: R. Taddeo R. Davitt 10101 9th Street North St. Petersburg, FL 33716		1	Pennsylvania State University Department of Mechanical Engineering ATTN: Dr. K. Kuo University Park, PA 16802
2	Olin Rocket Research Company ATTN: A. Harvey 11441 Willows Road, NE P.O. Box 97009 Redmond, WA 98073-9709		1	Renssalaer Polytechnic Institute Department of Math Sciences Troy, NY 12181
			1	University of Maryland ATTN: Dr. J.D. Anderson College Park, MD 20740
2	Rockwell International Science Center ATTN: Dr. S. Chakravarthy Dr. S. Palaniswamy 1049 Camino Dos Rios P.O. Box 1085 Thousand Oaks, CA 91360		3	University of Washington Aerospace and Energetics Research Program ATTN: Dr. A. Hertzberg Dr. A. Bruckner Dr. C. Knowlen
2	United Technologies Corporation Chemical Systems Division ATTN: Dr. R.O. MacLaren Mr. A.L. Holzman P.O. Box 49028 San Jose, CA 95161-9028			Seattle, WA 98195 Aberdeen Proving Ground
			1	Dir, USAMSAA ATTN: AMXSY-RA, R. Scungio
2	Veritay Technology, Inc. ATTN: S. Chandra E. Fisher 4845 Millersport Hwy. P.O. Box 305 East Amherst, NY 14051-0305		7	Cdr, CRDEC, AMCCOM ATTN: SMCCR-RSP-A, M. Miller
1	Director Johns Hopkins University Applied Physics Laboratory ATTN: Dr. Fred Billig Johns Hopkins Road Laurel, MD 20707			
1	North Carolina State University Mechanical and Aerospace Engineering Department ATTN: F.F. DeJarnette Raleigh, NC 27607			

No. of
Copies Organization

2   Institut Saint-Louis
      ATTN: Dr. F. Seiler
            Dr. Smeets
      F 68301 Saint-Louis Cedex
      12 rue de l'Industrie, B.P. 301
      France

USER EVALUATION SHEET/CHANGE OF ADDRESS

This laboratory undertakes a continuing effort to improve the quality of the reports it publishes. Your comments/answers below will aid us in our efforts.

1. Does this report satisfy a need? (Comment on purpose, related project, or other area of interest for which the report will be used.) _____

_____

_____

2. How, specifically, is the report being used? (Information source, design data, procedure, source of ideas, etc.) _____

_____

_____

3. Has the information in this report led to any quantitative savings as far as man-hours or dollars saved, operating costs avoided, or efficiencies achieved, etc? If so, please elaborate. _____

_____

_____

4. General Comments. What do you think should be changed to improve future reports? (Indicate changes to organization, technical content, format, etc.) _____

_____

_____

BRL Report Number ____BRL-TR-3222____   Division Symbol _____

Check here if desire to be removed from distribution list. ____

Check here for address change. ____

Current address: Organization _____

Address _____

_____